CONTENTS

INTRODUCTION

Over the past decades interaction of light with sub-wavelength structures still excites the minds of many scientists all around the world. A particular interest is attracted to resonant particles that posses relatively strong electric and magnetic response in the range of visible light spectrum. Generally speaking, these particles have unique properties to resonantly scatter incident light at a particular wavelength, as a result, becoming a prospective platform for various applications in nanophotonics [1; 2]. It is not surprising at all that there is side by side ongoing theoretical research in this area, mostly motivated by the breakthrough theory developed by Gustav Mie at the beginning of last century [3]. That being said, he proposed an approach to describe electromagnetic fields via the multipole series, as a result, explicitly connecting incident and scattered EM waves. Even more, one can directly implement this theory to compute optical forces and torques acting on a particle, as a result, motivating to investigate different optomechanical effects emerged for resonant nanoparticles. Therefore, the following thesis is devoted to the applications of resonant nanoparticles in optical trapping [4] and in non-linear optics [5; 6].

The fascinating story of optical trapping experienced a huge boost around fifty years ago starting from the pioneer works by Arthur Ashkin [7—9] that allowed him to get the Nobel Prize in 2018. One of his breakthrough results defined a condition for a nanoparticle to be trapped by a highly-focused single Gaussian beam [10]. As illustrated in Fig. 1, a particle experiences two forces coming from the laser radiation focused by the microscope objective. The scattering force F_{scat} represents the radiative pressure force that takes the particle out of the trap and competes with the gradient force F_{grad} that emerges due to the laser intensity profile close to the beam focus center. Therefore, when the ratio of the backward-gradient force to the forward-scattering force is greater than 1, the stable trapping

at $z_{\text{eq}} = \frac{\pi w_0^2}{\sqrt{3}\lambda}$ by single Gaussian beam with w_0 waist and wavelength λ was successfully demonstrated [10].

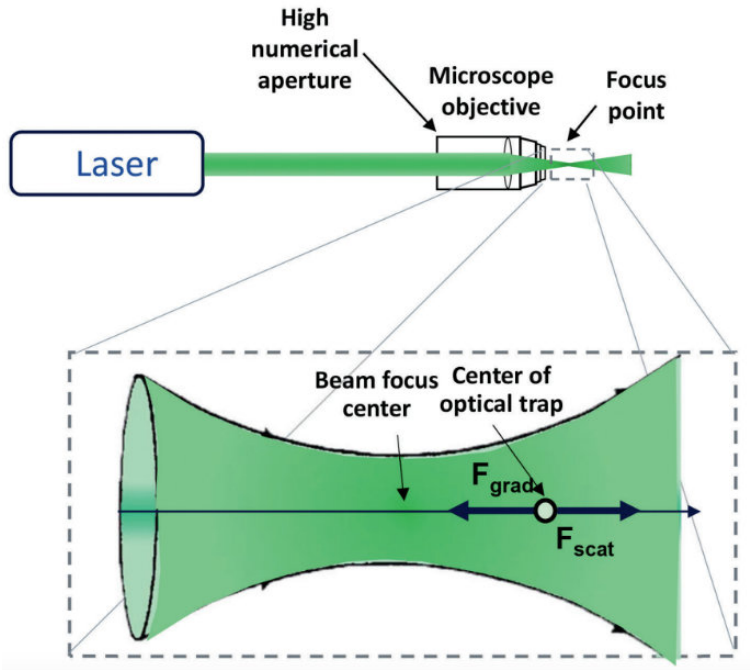

Figure 1 — a) Schematic optical tweezer setup to trap a particle close to the beam focus center. Laser light focused by a microscope objective creates an intensity profile leading to the emergence of the gradient force. At equilibrium position, the gradient and scattering forces cancel out. The Fig. is reproduced from the Nobel Prize Lecture given by A. Ashkin in 2018 [11]

Today it is almost impossible to imagine any experimental setup for studying and manipulating single nanoparticles or molecules without optical trapping techniques. These days optical tweezers are actively used in biology [12; 13], for instance, addressing the nature of interactions between DNA and proteins as well as their mechanical properties [14]. Even more, optical traps are well-integrated with commercially available microscopes, as a result, providing a platform for efficient and robust cell-sorting methods [15; 16]. At the same time, optical tweezers can be implemented to create arbitrary three-dimensional traps to localise structured arrays of nanoparticles and perform dynamical computer control [18]. This approach is actively used in quantum computing [17] opening new directions to study many-body physics as well as to use Rydberg atoms as single-qubits [19],

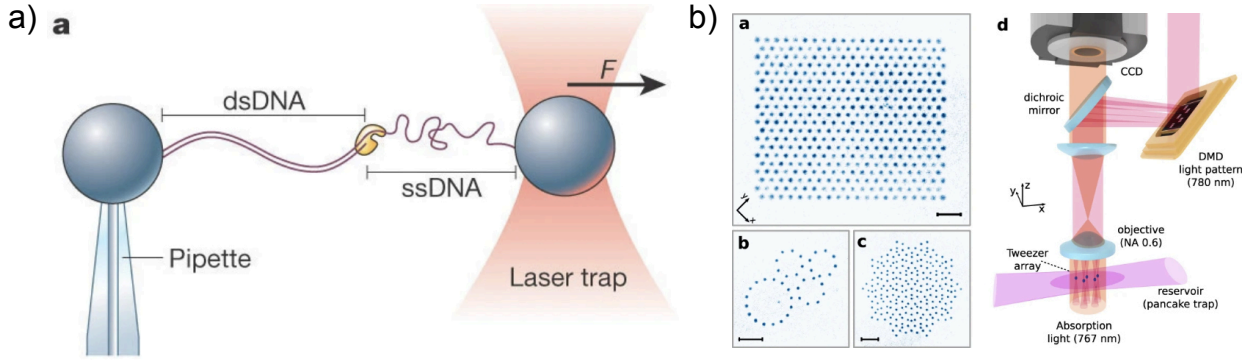

Figure 2 — a) DNA molecule trapped by an optical tweezer and a micropipette allows to measure mechanical extension associated with dsDNA and ssDNA [14]. b) Ultracold atoms trapped in tweezer system can form different optical lattice configurations to simulate quantum many-body systems [17]

therefore, being one of the most crucial parts for prospective trapped-ion quantum computers [20; 21].

Moreover, over the past years optical levitation has been actively developing both theoretically and experimentally. For instance, the feedback cooling technique was presented for optically levitated silica nanoparticle by measuring its position via a SiN membrane, therefore, resulting in new methods to investigate short-range interactions [22]. In addition, cooling of a levitated nanoparticle to its motional quantum ground state was recently demonstrated [23], therefore, providing new methods for sensing as well as for exploring fundamental questions in physics. At the same time, conventional trapping at the Gaussian beam focus center has several disadvantages that become extremely crucial for optical levitation. That being said, high laser intensity can generate external noise, as a result, leading to errors in delicate measurements, sensing and motional ground state cooling. Even more, strong laser fields might damage or overheat living cells or nanoparticles. Therefore, one could try to avoid high laser intensity and trap a nanoparticle at low-intensity spot in order to decrease its internal temperature. Due to the resonant behaviour of the Mie-particle polarizabilities, one can use a standing wave trap and locate a particle at the node of the electric field [4]. However, since at the same time, the magnetic field reaches its maximum value, external noise

and overheating still remain to be a problem. For these reasons, in our work we address recently proposed bottle-beam trap formed by two destructively interfering Gaussian beams, where there is a spot with no electric and magnetic fields at all [24].

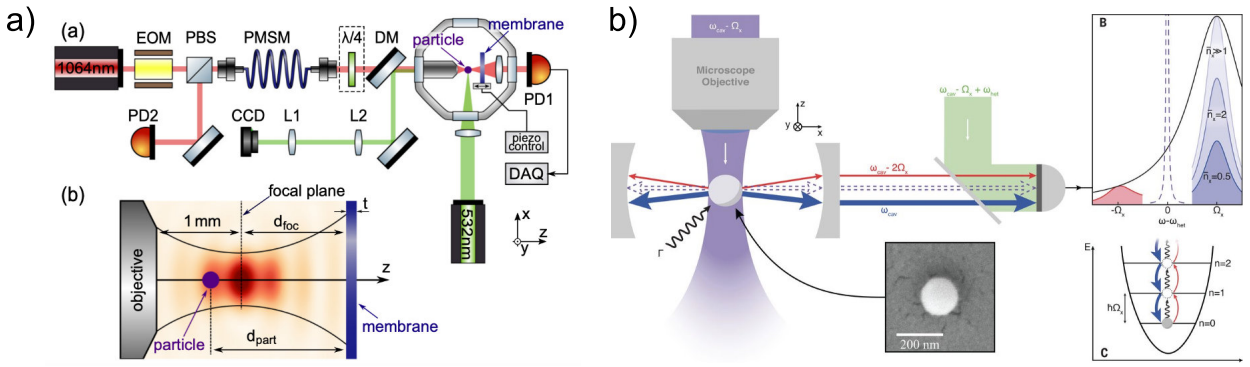

Figure 3 — a) Optically levitated silica nanoparticle at a distance of 380 nm from a SiN membrane provides a platform to achieve feedback cooling as well as to characterize the particle's position via the interferometric technique [22]. b) Spherical silica nanoparticle trapped by an optical tweezer. Stokes scattering processes (heating) are suppressed, while Anti-Stokes (cooling) are enhanced, as a result, cooling to the quantum motional ground state was demonstrated [23]

At the same time, resonant nanoparticles open novel opportunities for optical rotation as well rather than just for trapping. That being said, conventionally it is impossible to rotate a perfect spherical nanoparticle without any losses due to the angular momentum conservation between the incident and scattered light. In order to overcome this problem, one can either break the rotational symmetry [25; 26] or introduce the Ohmic losses [27; 28] for the particle. In other words, both these approaches violate the conservation of total angular momentum, as a result, making it possible to rotate a particle. Resonant nanoparticles allows us to propose a novel approach to transfer angular momentum to a non-absorbing particle via the second-harmonic generation. In other words, it is possible to induce rotation on a perfectly spherical nanoparticle by exploiting its crystal structure symmetry leading to the emergence of the second harmonic scattered field.

Finally, the main tasks we address in this thesis are the following:

1. Investigate a standing wave trap as the simplest platform to achieve trapping of a resonant nanoparticle at minimum intensity spot.
2. Compute the total force acting on the nanoparticle trapped at the node of the electing field in the standing wave, analyse the contribution of the different multipole terms, define the condition for the nanoparticle to be stably trapped.
3. Study the formation of the bottle-beam trap created by two Gaussian beams, identify the position area where low-intensity trapping is desired.
4. Calculate the total axial and transverse forces acting on the nanoparticle at minimum intensity spot, distinguish the main multipole terms that provide stable trapping.
5. Investigate the emergence of optical torque acting on a resonant spherical nanoparticle with negligible losses induced by the second harmonic generation.

1. OPTICAL TRAPPING. OVERVIEW

The following chapter is devoted to the review on the basic principles of optical trapping. Namely, one can define a dimensionless parameter as a ratio of a particle radius a and the wavelength of a trapping beam λ. That being said, when $a/\lambda \gg 1$ one can use the principles of geometrical optics to explain optical trapping as will be discussed below in Section 1.1. For $a/\lambda \gg 1$, the Rayleigh approximation provides a powerful tool to calculate the gradient and scattered forces acting on a nanoparticle, as a result, defining the position of stable trapping. Finally, to address the last missing case, in other words, $a/\lambda \approx 1$, we discuss the generalized Lorentz-Mie theory and the T-matrx approach as a quite robust method to calculate an optical force beyond the geometrical and Rayleigh approximations.

1.1 Geometrical optics

The first approach to explain the effect of optical trapping is based on simple geometrical optics principles. As was mentioned above, this method is particularly useful when the particle radius a is much larger compared to the wavelength λ of a trapping Gaussian beam. For instance, if we assume λ to lie in the range of visible light, the size of a nanoparticle in this case should be around several microns to fulfil the basic assumptions of ray optics. To be more precise, Fig. 1.1 shows a nanoparticle placed close to the focus center of a single Gaussian beam. Naturally, in order to achieve stable trapping in all directions, we can take into account the axial symmetry of the beam and divide this question into two subparts, namely, in horizontal and vertical trappings.

Both horizontal and vertical trappings can be explained in the limit of geometrical optics based on the total momentum conservation. As schematically illustrated in Fig.1.1 a), a particle shifted to the left (horizontally) from the beam focus experiences recoil momentum transferred from the difference between incident and scattered light rays. The direction of recoil momentum points towards the beam focus center, as a result, returning the particle back to the trapping

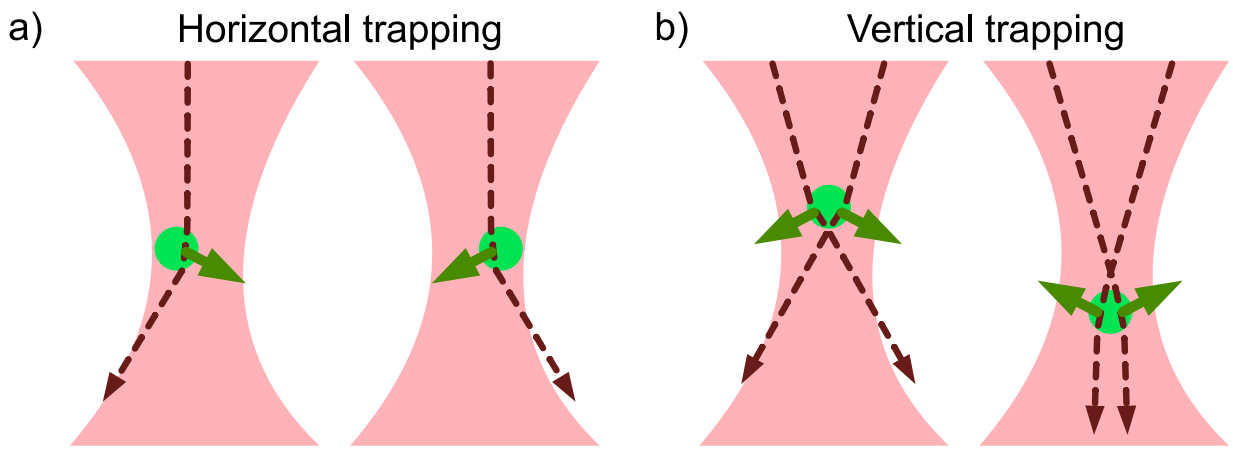

Figure 1.1 — a) Horizontally and b) vertically shifted particle experiences the recoil force to the beam focus center coming from the difference in incident and scattered light momenta. Dashed red lines represent the beam rays, green solid arrows stand for the recoil force direction

position. At the same time, if one shifts the particle horizontally to the right, the corresponding recoil force coming from transferred momentum acts in an opposite way, that being said, pointing to the left. As a result, the particle returns back to the beam focus and horizontal trapping is fulfilled.

Almost the same argument holds for vertical trapping as demonstrated in Fig.1.1 b), where the particle is shifted above/below the beam focus center. Therefore, one can easily check that the recoil force in this particular case coming from transferred momentum will return the particle back to the focus spot. To be more precise, two green arrows in Fig.1.1 b) represent the recoil force components that, as in the horizontal trapping analysis discussed above, appear due to the momenta difference. Combining these recoil forces together leads to the vertical force pointing up/down for a shift below/up the focus spot, thus, providing vertical trapping.

The reader might have a strong feeling that geometrical optics doesn't sound like a valid and solid way to explain the effect ot optical trapping. Even though ray optics don't contain any information regarding the spin or a phase of light, we would like to reveal this concern. Despite of the restrictions coming from the basic assumptions in geometrical optics, one can use this approach to confirm the

existence of negative optical forces [29], forces acting on absorbing particles [30] as well as on Janus particles [31]. Therefore, this approach allows to obtain not only qualitative, but also quantitative results.

1.2 Rayleigh approximation

When the size of a trapping particle is much smaller compared to the wavelength λ of a Gaussian beam that forms an optical trap, one can use the Rayleigh approximation, in other words, the single dipole approximation. In this case, the total force acting on the particle is formed by the gradient force as well as by the scattering force as was demonstrated by A. Ashkin in his works [9; 10]. The gradient force is directly proportional to the particle's polarizability and acts like a recoil force that returns the particle back to the focus center of the beam. At the same time, the scattering force associated with the imaginary part of the polarizability acts in the opposite way, namely, taking the particle out of the beam focus and competing with the gradient force. As a result, the equilibrium position for the particle being trapped corresponds to the configuration when both these forces cancel out and the total force is zero.

To proceed further, Fig. 1.2 shows a particle trapped in a single Gaussian beam as well as the gradient $\mathbf{F}_{\text{grad}}$ and scattering forces $\mathbf{F}_{\text{scat}}$. Since the optical forces are strongly related to the electric and magnetic fields, one can use the paraxial approximation to represent EM-fields in the following way:

$$\begin{cases} \mathbf{E}(r,z) = E_0\,\hat{\mathbf{e}}_x\,\frac{w_0}{w(z)}\exp\left(-\frac{r^2}{w(z)^2}\right)\exp\left(-i\left(kz + k\frac{r^2}{2R(z)} - \psi(z)\right)\right) \\ \mathbf{B}(r,z) = B_0\,\hat{\mathbf{e}}_y\,\frac{w_0}{w(z)}\exp\left(-\frac{r^2}{w(z)^2}\right)\exp\left(-i\left(kz + k\frac{r^2}{2R(z)} - \psi(z)\right)\right) \end{cases}, \quad (1.1)$$

where $k = \frac{2\pi}{\lambda}$ is the wavevector, r and z are radial and axial distances to the beam focus center, respectively, w_0 corresponds to the beam waist at the focus center,

$$R(z) = z\left(1 + \left(\frac{z_{\text{R}}}{z}\right)^2\right) \quad (1.2)$$

is the curvature radius of the Gaussian beam wavefront,

$$w(z) = w_0\sqrt{1 + \left(\frac{z}{z_{\text{R}}}\right)^2} \quad (1.3)$$

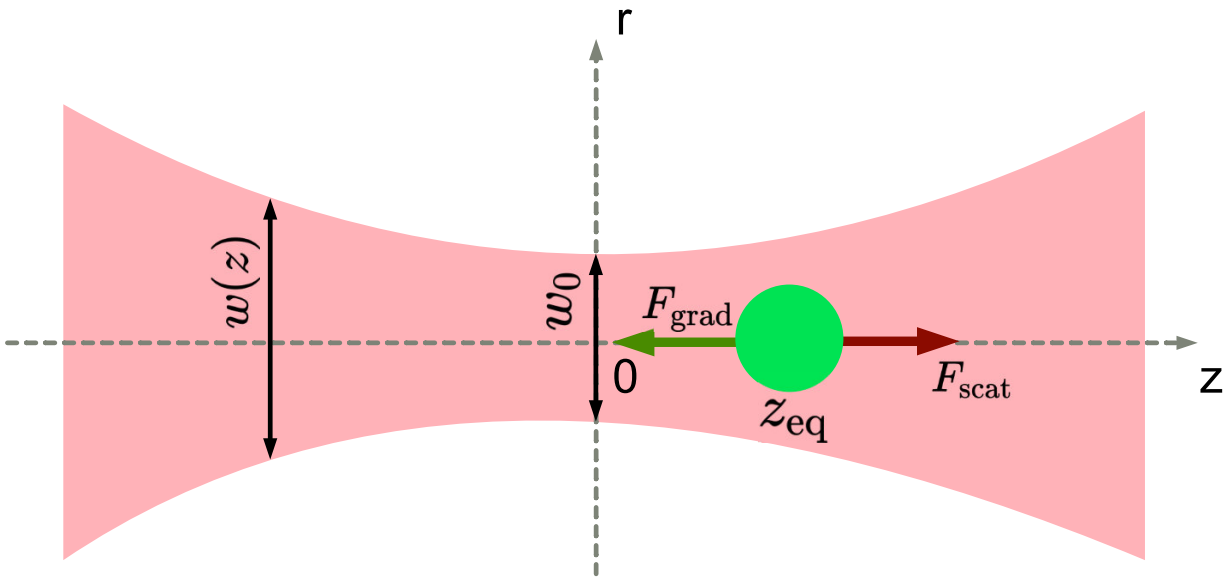

Figure 1.2 — Gaussian beam oriented along z-axis and focused at $z = 0$. The beam waist at the focus center is equal to w_0 and changes along z direction as $w(z)$. A particle trapped by the beam experience competing gradient $\mathbf{F}_{\text{grad}}$ and scattering $\mathbf{F}_{\text{scat}}$ forces, that should have the same amplitude at z_{eq} particle's position

is the beam waist when the field amplitude decreases by e times at $z = z_R = \frac{\pi w_0^2 n}{\lambda}$ distance along z-direction called the Rayleigh range. Here n is the refractive index of the medium around, that for simplicity can be set to 1 (vacuum), while

$$\psi(z) = \arctan z/z_R \tag{1.4}$$

is the Gouy phase at z-position.

Therefore, one can consider a lossless particle with radius $a \ll \lambda$ and the refractive index n_p placed into the Gaussian beam with peak intensity at $z = 0$ focus spot being equal to I_0. In this case, the scattering force $\mathbf{F}_{\text{scat}}$ acting on the nanoparticle takes the following form [10]:

$$\mathbf{F}_{\text{scat}} = \frac{n_p P_{\text{scat}}}{c} = \frac{I_0}{c}\frac{128\pi^5 a^6}{3\lambda^4}\left(\frac{m^2-1}{m^2+2}\right)^2 n_p \cdot \frac{\mathbf{k}}{k}, \tag{1.5}$$

where $m = n_p/n$ being the relative refractive index between the particle and surrounding medium, $\mathbf{k}$ represents the trapping beam wavevector. Next, as was mentioned above, the gradient force $\mathbf{F}_{\text{grad}}$ can be written via the particle's

polarizability α in the dipole approximation as:

$$\mathbf{F}_{\text{grad}} = -\frac{n_p}{2}\alpha\nabla\mathbf{E}^2 = -\frac{n_p^3 a^3}{2}\left(\frac{m^2-1}{m^2+2}\right)\nabla\mathbf{E}^2. \tag{1.6}$$

As a result, in order to achieve the axial trapping (along z-direction), the forces acting on the particle at the equilibrium spot z_{eq} must follow:

$$0 = F_z^{\text{total}}(0,z_{\text{eq}}) = F_z^{\text{scat}}(0,z_{\text{eq}}) + F_z^{\text{grad}}(0,z_{\text{eq}}). \tag{1.7}$$

Finally, one can show that at the equilibrium position z_{eq} along z-axis the ratio between axial scattering and gradient forces takes the following form:

$$\frac{F_z^{\text{scat}}}{F_z^{\text{grad}}} = \frac{64\pi^5}{3\sqrt{3}} \cdot \frac{m^2-1}{m^2+2}\frac{w_0^2 a^3}{n_p^2 \lambda^5}, \tag{1.8}$$

therefore, recalling the limit $a \ll \lambda$ we are working with in this subsection, it is clearly seen that the scattering force can be sufficiently suppressed. As a result, due to the dominating contribution of the gradient force, the particle can be trapped along z-direction. Almost the same arguments hold for radial trapping as well [10].

1.3 T-matrix approach

Up to the moment we have discussed two limits: $a \gg \lambda$ that corresponds to the geometrical optics approach as well as $a \ll \lambda$ that can be resolved via the dipole approximation following the Rayleigh formalism. Therefore, the last case we are missing out is $a \approx \lambda$. One of the ways to describe the effect of optical trapping in this particular case is the generalized Lorenz–Mie theory (GLMT) [32]. While the well-known Mie-Lorenz scattering theory [3] addresses scattering phenomena of a spherical particle illuminated by an incident plane wave, the GLMT extends this approach to an arbitrary incident wave, and, for instance, can be implemented for a Gaussian beam one usually deals with for an optical trap. It is worth mentioning that one can obtain the corrections for the paraxial approximation [33] we discussed above, therefore, naturally connecting the dipole approximation with the $a \approx \lambda$ case.

While the GLMT itself is rather analytical approach, its natural extension to a direct numerical method that allows to investigate trapping at $a \approx \lambda$ is based on the T-matrix formalism, generally speaking, by addressing the scattered EM fields. Namely, one can decompose the incident and scattered electric fields into vector spherical harmonics (VSH) [34] in the following way:

$$\begin{cases} \mathbf{E}^{\text{inc}} = \sum\limits_{n=1}^{\infty} \sum\limits_{m=-n}^{n} a_{nm}\mathbf{M}_{nm}^{(2)} + b_{nm}\mathbf{N}_{nm}^{(2)} \\ \mathbf{E}^{\text{scat}} = \sum\limits_{n=1}^{\infty} \sum\limits_{m=-n}^{n} p_{nm}\mathbf{M}_{nm}^{(1)} + q_{nm}\mathbf{N}_{nm}^{(1)}, \end{cases} \tag{1.9}$$

where $\mathbf{M}_{nm}^{(1,2)}, \mathbf{N}_{nm}^{(1,2)}$ are complex spherical vector harmonics based on the Hankel spherical functions of the first and second kinds that correspond to the magnetic and electric multipoles, respectively. Then, the T-matrix connects expansion coefficients a_{nm}, b_{nm} of an incident wave with the scattered ones p_{nm}, q_{nm} in the following way:

$$\begin{pmatrix} \dots \\ p_{mn} \\ \dots \\ q_{nm} \\ \dots \end{pmatrix} = T \cdot \begin{pmatrix} \dots \\ a_{mn} \\ \dots \\ b_{nm} \\ \dots \end{pmatrix}. \tag{1.10}$$

The key idea here is that the T-matrix itself depends only on the properties of an object that scatters the light (such as, for instance, its shape, size, refractive index) as well as on the wavelength of incident light. Therefore, if one manages to compute ones the T-matrix elements, then it can be used for an arbitrary incident field by defining a_{nm}, b_{nm} expansion coefficients and computing p_{nm}, q_{nm} for the scattered field just by simple matrix multiplication. Since we are mostly interested in spherical particles for this thesis, then, following the GLMT the T-matrix will be just diagonal and formed by the corresponding Mie-coefficients that can be easily calculated numerically [34].

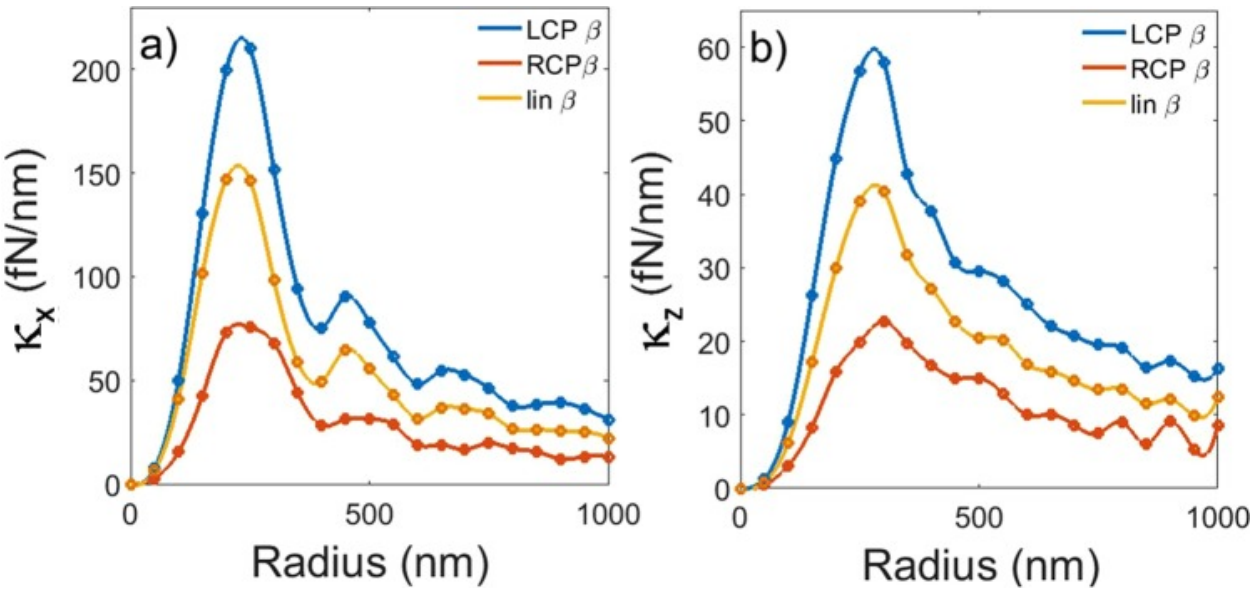

Figure 1.3 — a) Transverse and b) axial trapping stiffnesses as a radius of an optically active particle. β states for the chirality of the incident light polarization and distinguish between left-hand circular polarization (blue curve), right-hand circular polarization (red curve) and linear polarization (yellow curve). The Fig. is reproduced from [35]

Finally, given the T-matrix one can express the total axial force acting on a particle in the following way [36]:

$$F_z = F_z^1 + F_z^2, \tag{1.11}$$

where

$$F_z^1 = \frac{2n}{c}\sum_{n=1}^{\infty}\sum_{m=-n}^{n}\frac{m}{n(n+1)}\Re\left(a_{nm}^* b_{nm} - p_{nm}^* q_{nm}\right) \tag{1.12}$$

and

$$F_z^2 = \frac{2n}{c}\sum_{n=1}^{\infty}\sum_{m=-n}^{n}\beta_{nm}\frac{m}{n(n+1)}\times \tag{1.13}$$

$$\times\Re\left(a_{nm}a_{n+1,m}^* + b_{nm}b_{n+1,m}^* - p_{nm}p_{n+1,m}^* - q_{nm}q_{n+1,m}^*\right), \tag{1.14}$$

with the factor β_{nm} defined as:

$$\beta_{nm} = \frac{1}{n+1}\sqrt{\frac{n(n+2)(n-m+1)(n+m+1)}{(2n+1)(2n+3)}}. \tag{1.15}$$

That being said, the force F_z^1 is associated with interfering multipoles with the same n,m numbers, while F_z^2 represents the terms with the same m and different n. To

obtain the F_x and F_y components of the total force, one can rotate the coordinate system by 90° such that x- or y-axis coincide with z-axis, use the expression presented above and rotate the coordinate system back.

In order to provide a concrete example how the T-matrix approach can be implemented in order to calculate the forces acting on a particle, we suggest the following work [35]. To be more precise, the authors performed modelling of optical tweezers based on the chiral incident beams to trap optically active particles [37]. As a main result, they were able to develop the chiral T-matrix method to compute transverse and axial trapping stiffnesses (we will discuss the stiffness definition in Section 1.5) as illustrated in Fig. 1.3 for circularly and linearly polarized incident light. It is worth mentioning that the proposed approach can be extended to the modelling of optical forces acting on the optically active living cells [35].

1.4 Multipole-based force calculation

In the following section we discuss the approach to calculate an optical force based on the multipole decomposition. To start with, the time-averaged optical force can be expressed in the following way:

$$\langle \mathbf{F} \rangle = \frac{1}{2} \Re \oint_S \hat{\mathcal{T}} \cdot \mathbf{n} dS, \tag{1.16}$$

where the integration is performed over a surface S, and $\mathcal{T}$ is the Maxwell's stress tensor defined as:

$$\hat{\mathcal{T}} = \frac{1}{2} \Re \left(\varepsilon \varepsilon_0 \mathbf{E}^* \otimes \mathbf{E} + \mu \mu_0 \mathbf{H}^* \otimes \mathbf{H} - \frac{1}{2} \left(\varepsilon \varepsilon_0 |\mathbf{E}|^2 + \mu \mu_0 |\mathbf{H}|^2 \right) \hat{\mathcal{I}} \right), \tag{1.17}$$

where $\mathbf{E} = \mathbf{E}^{\text{inc}} + \mathbf{E}^{\text{scat}}$ and $\mathbf{H} = \mathbf{H}^{\text{inc}} + \mathbf{H}^{\text{scat}}$ are the total electric and magnetic fields, respectively, formed by incident and scattered light. Next, using the far-field multipolar decomposition [38] one can represent the total force $\langle \mathbf{F} \rangle$ as a sum of the extinction force $\langle \mathbf{F}^{\text{ext}} \rangle$ and the recoil force $\langle \mathbf{F}^{\text{ext}} \rangle$ [39], namely:

$$\langle \mathbf{F} \rangle = \langle \mathbf{F}^{\text{ext}} \rangle + \langle \mathbf{F}^{\text{rec}} \rangle. \tag{1.18}$$

Performing the integration over the Maxwell's stress tensor presented above results in the following expression for the extinction force, where incident and scattered fields are mixed:

$$\langle \mathbf{F}^{\text{ext}} \rangle = -\frac{1}{2} \lim_{r\to\infty} \oint_S \left(\varepsilon_0 \mathbf{E}_{\text{inc}} \cdot \mathbf{E}^*_{\text{scat}} + \mu_0 \mathbf{H}_{\text{inc}} \cdot \mathbf{H}^*_{\text{scat}} \right) dS, \tag{1.19}$$

at the same time, following the same steps leads to the expression for the recoil force where only scattered fields are involved:

$$\langle \mathbf{F}^{\mathbf{rec}} \rangle = -\frac{1}{4} \lim_{r\to\infty} \oint_S \Re \left(\left(\varepsilon_0 \mathbf{E}_{\text{scat}} \cdot \mathbf{E}^*_{\text{scat}} + \mu_0 \mathbf{H}_{\text{scat}} \cdot \mathbf{H}^*_{\text{scat}} \right) \cdot \mathbf{n} \right) dS. \tag{1.20}$$

To proceed further, one can decompose the forces presented above into different multipoles. That being said, the extinction force $\mathbf{F}^{\text{ext}}$ can be represented as a sum of electric dipole (ED), magnetic dipole (MD), electric quadrupole (EQ) and magnetic quadrupole(MQ) forces as follows:

$$\langle F_i^{\text{ext}} \rangle = \langle F_i^{ED} \rangle + \langle F_i^{MD} \rangle + \langle F_i^{EQ} \rangle + \langle F_i^{MQ} \rangle, \tag{1.21}$$

where the expressions for each multipole force are presented below:

$$\begin{cases} \langle F_i^{ED} \rangle = \frac{1}{2} \Re \left(p_j \nabla_i E_j^* \right) \\ \langle F_i^{MD} \rangle = \frac{1}{2} \Re \left(m_j \nabla_i B_j^* \right) \\ \langle F_i^{EQ} \rangle = \frac{1}{4} \Re \left(Q^e_{jk} \nabla_i \nabla_k E_j^* \right) \\ \langle F_i^{MQ} \rangle = \frac{1}{4} \Re \left(Q^m_{jk} \nabla_i \nabla_k B_j^* \right). \end{cases} \tag{1.22}$$

Here we use the induced electric $\mathbf{p}$ and magnetic $\mathbf{m}$ dipole moments defined via the corresponding Mie-polarizablities α_{ED} and α_{MD}, respectively, as:

$$\begin{cases} \mathbf{p} = \varepsilon_0 \alpha_{ED} \mathbf{E}_{\text{inc}} \\ \mathbf{m} = \alpha_{MD} / \mu_0 \mathbf{B}_{\text{inc}} \end{cases}, \tag{1.23}$$

while the quadrupole moments for the electric and magnetic multipoles are the following:

$$\begin{cases} \mathbf{Q}^e = \varepsilon_0 \alpha_{EQ} \frac{\nabla \mathbf{E}_{\text{inc}} + \mathbf{E}_{\text{inc}} \nabla}{2} \\ \mathbf{Q}^m = \alpha_{MQ} / \mu_0 \frac{\nabla \mathbf{B}_{\text{inc}} + \mathbf{B}_{\text{inc}} \nabla}{2} \end{cases}. \tag{1.24}$$

According to [34], the Mie-polarizabilities are directly related to the Mie-coefficients $\{a_1,a_2,b_1,b_2\}$ as:

$$\begin{cases} \alpha_{ED} = i\frac{6\pi}{k^3}a_1 \\ \alpha_{MD} = i\frac{6\pi}{k^3}b_1 \\ \alpha_{EQ} = i\frac{40\pi}{k^5}a_2 \\ \alpha_{MQ} = i\frac{40\pi}{k^5}b_2 \end{cases} \tag{1.25}$$

A similar idea holds for the recoil force, namely, one can represent the total force as a sum of electric dipole - magnetic dipole force (ED-MD), electric dipole - electric quadrupole force (ED-EQ), magnetic dipole - magnetic quadrupole force (MD-MQ) as well as electric quadrupole - magnetic quadrupole force (EQ-MQ):

$$F_i^{\text{rec}} = F_i^{ED-MD} + F_i^{ED-EQ} + F_i^{MD-MQ} + F_i^{EQ-MQ}. \tag{1.26}$$

The expressions for these interference forces are listed below and their names are strongly connected with the corresponding dipole/quadrupole moments that are involved in each particular force term:

$$\begin{cases} \langle F_i^{ED-MD} \rangle = -\frac{k^4}{12\pi\varepsilon_0 c}\Re\left(\varepsilon_{ijk}p_j m_k^*\right) \\ \langle F_i^{ED-EQ} \rangle = -\frac{k^5}{40\pi\varepsilon_0}\Im\left(Q_{ij}^e p_j^*\right) \\ \langle F_i^{MD-MQ} \rangle = -\frac{k^5}{40\pi\varepsilon_0 c^2}\Im\left(Q_{ij}^m m_j^*\right) \\ \langle F_i^{EQ-MQ} \rangle = -\frac{k^6}{240\pi\varepsilon_0 c}\Re\left(\varepsilon_{ijk}p_j m_k^*\right) \end{cases}. \tag{1.27}$$

Therefore, now we are able to compute the total force acting on a particle as well as to perform analysis on what multipole force dominates in each particular case. One can clearly notice that all the forces presented above strongly depends on the corresponding Mie-polarizabilities.

1.5 Trap stiffness

In the previous sections we discussed several approaches how to calculate the total optical force acting on a particle. Next, a quite natural question arises:

how to define whether our particle is indeed trapped by an optical tweezer. The first intuitive condition is that the total force must be equal to 0 at the trapping spot. However, if we consider more realistic cases where positioning a particle precisely at one desired spot is almost impossible, particular behaviour of the total force at the trapping position seems to be a necessary requirement to achieve stable trapping. In other words, if one focuses for the moment on the axial trapping at $z = 0$, then for the particle's position at $z > 0$ the total force should be negative, while at $z < 0$ the force is required to be positive. As a result, in both cases the total force returns the particle back to the trapping spot in the optical tweezers.

To generalize this statement and characterize the trapping stability as well as its strength, one can use axial and radial trap stiffnesses κ_z and κ_r, respectively, defined in the following way:

$$\kappa_z = -\partial_z F_z, \quad \kappa_r = -\partial_r F_r, \tag{1.28}$$

where F_z and F_r represent for the axial and radial force components. In other words, we have:

$$F_z\big|_{z=0} \approx -\kappa_z \cdot z, \quad F_r\big|_{r=0} \approx -\kappa_r \cdot r. \tag{1.29}$$

Finally, taking into account the argument on the total force sign at $z > 0$ and $z < 0$, we obtain stable trapping for positive stiffness $\kappa > 0$, while for $\kappa < 0$ trapping is unstable even though the total force might be equal to zero.

2. STANDING WAVE TRAP

The main purpose of the following chapter is to investigate an optical trap formed by a standing wave. As was stated before, we want to trap a Mie-resonant nanoparticle in minimum intensity spot, and, without loss of generality, we consider trapping at the node of the electric field. By the end of this chapter we want to answer the following question: what wavelength λ of the standing wave and particle's radius R one could use to trap a Mie-resonant particle by the standing wave. The corresponding condition to obtain stable trapping, as was presented in Section 1.5, is defined via the trap stiffness κ, namely, whether its value is positive or negative.

2.1 Trap formation

To begin with, we consider a standing wave oriented along z-axis with wavevector $k = \frac{2\pi}{\lambda}$. For our further convenience, we assume the electric field $\mathbf{E}$ to be polarized along x-axis, while the magnetic field $\mathbf{B}$ is oriented along y-axis (as illustrated in Fig. 2.1). Next, since one can represent the E-components of the forward (f) and backward (b) propagating waves in the following way:

$$E_x^f(z,t) = \frac{E_0}{2} \cdot \cos(kz - \omega t) \quad \text{and} \quad E_x^b(z,t) = -\frac{E_0}{2} \cdot \cos(-kz - \omega t), \quad (2.1)$$

then, the total electric field can be written as:

$$E_x(z,t) = E_x^f(z,t) + E_x^b(z,t) = E_0 \sin kz \sin \omega t. \quad (2.2)$$

At the same time, the magnetic field components along y-direction for (f) and (b) waves are equal to :

$$B_y^f(z,t) = \frac{B_0}{2} \cdot \cos(kz - \omega t) \quad \text{and} \quad B_y^b(z,t) = \frac{B_0}{2} \cdot \cos(-kz - \omega t), \quad (2.3)$$

as a result, the total magnetic field takes the following form:

$$B_y(z,t) = B_y^f(z,t) + B_y^b(z,t) = B_0 \cos kz \cos \omega t, \quad (2.4)$$

and, as expected, experiences a $\pi/2$ shift with respect to the electric field $E_x(z,t)$.

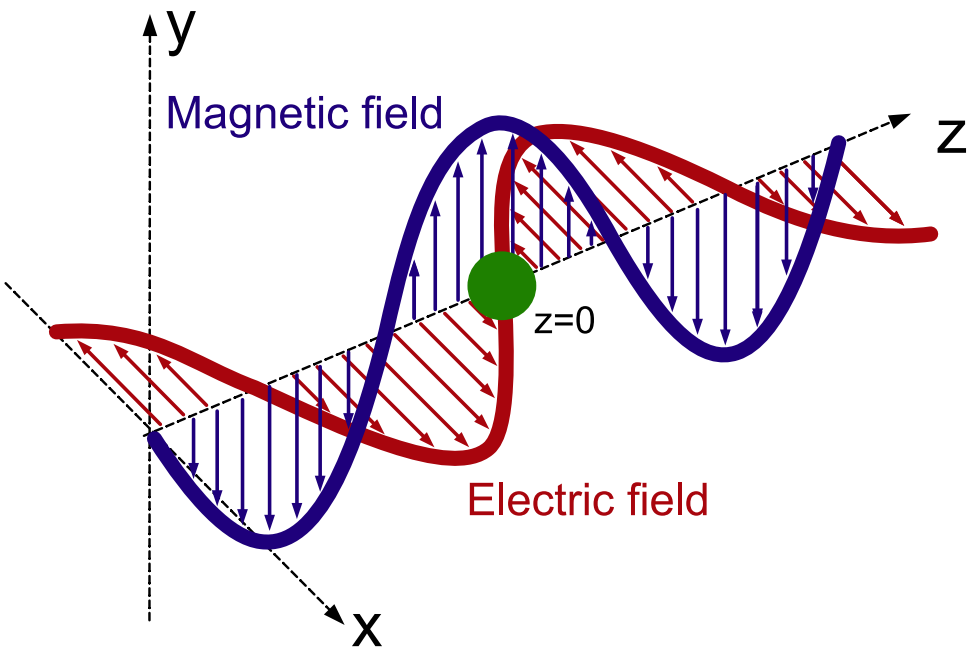

Figure 2.1 — The standing wave formed along z-axis, electric and magnetic fields are polarized along x- and y- axes, respectively, and posses a relative $\pi/2$ shift. Mie-nanoparticle (green circle) is trapped in the node of the electric field, $z = 0$

Next, we take into account the fact that in a standing wave the scattering forces acting on a nanoparticle from the forward and backward propagating waves just cancel out. Therefore, there is no recoil components of the total force acting on the nanoparticle. As a result, the expression of the total force simplifies into:

$$\langle F_i^{\text{total}} \rangle = \langle F_i^{ED} \rangle + \langle F_i^{MD} \rangle + \langle F_i^{EQ} \rangle + \langle F_i^{MQ} \rangle, \tag{2.5}$$

where we consider the contribution of electric dipole (ED), magnetic dipole (MD), electric quadrupole (EQ) as well as magnetic quadrupole (MQ). Overall, we need to calculate explicitly the following terms:

$$\begin{cases} \langle F_i^{ED} \rangle = \frac{1}{2} \langle \Re \left(p_j \nabla_i E_j^* \right) \rangle \\ \langle F_i^{MD} \rangle = \frac{1}{2} \langle \Re \left(m_j \nabla_i B_j^* \right) \rangle \\ \langle F_i^{EQ} \rangle = \frac{1}{4} \langle \Re \left(Q_{jk}^e \nabla_i \nabla_k E_j^* \right) \rangle \\ \langle F_i^{MQ} \rangle = \frac{1}{4} \langle \Re \left(Q_{jk}^m \nabla_i \nabla_k B_j^* \right) \rangle. \end{cases} \tag{2.6}$$

2.2 Dipole forces

At first, we discuss the electric and magnetic dipole forces. Since only x-component of the total electric field is non-zero (see Fig. 2.1) while its derivative is only non-zero with respect to z (according to 2.2), the electric dipole force $\langle \mathbf{F}^{ED} \rangle = \langle F_z^{ED} \rangle \cdot \mathbf{e}_z$ in 2.6 can be written as:

$$F_z^{ED} = \frac{1}{2} \langle \Re \left(p_x \nabla_z E_x^* \right) \rangle. \tag{2.7}$$

Substituting into 2.7 the expression for the electric dipole moment equals $p_x = \varepsilon_0 \alpha_{ED} E_0 \sin kx \sin \omega t$ (defined via the corresponding Mie-polarizability α_{ED}), we have:

$$F_z^{ED} = \frac{1}{2} \langle \Re \left(\varepsilon_0 \alpha_{ED} E_0 \sin kz \sin \omega t \cdot k \cdot E_0 cos kz \sin \omega t \right) \rangle = \\ = \frac{1}{8} \varepsilon_0 \Re(\alpha_{ED}) k E_0^2 \sin 2kz. \tag{2.8}$$

Next, we compute the magnetic dipole force in a similar way, recalling two facts: 1) only y-component of the total magnetic field is non-zero and 2) its derivatives with respect to x and y vanish. As a result, we get the following expression for the magnetic dipole force $\langle \mathbf{F}^{MD} \rangle = \langle F_z^{MD} \rangle \cdot \mathbf{e}_z$:

$$\langle F_z^{MD} \rangle = \frac{1}{2} \langle \Re \left(m_y \nabla_z E_x^* \right) \rangle = -\frac{1}{8} \frac{\Re(\alpha_{MD})}{\mu_0} k B_0^2 \sin 2kz, \tag{2.9}$$

where we substitute the magnetic dipole moment as $m_y = \frac{\alpha_{MD}}{\mu_0} E_0 \sin kx \sin \omega t$. Finally, the total force generated by the electric and magnetic dipoles can be written as:

$$\langle F_z^D \rangle = \langle F_z^{ED} \rangle + \langle F_z^{MD} \rangle = \frac{1}{8} \varepsilon_0 \Re(\alpha_{ED}) k E_0^2 \sin 2kz - \frac{1}{8} \frac{\Re(\alpha_{MD})}{\mu_0} k B_0^2 \sin 2kz. \tag{2.10}$$

2.3 Quadrupole forces

Now we want to compute the forces coming from the electric and magnetic quadrupoles. Recalling the expressions presented in 2.6, only z-component of the

electric quadrupole force is nonzero and equals:

$$\langle F_z^{EQ} \rangle = \frac{1}{4} \langle \Re \left(Q_{xz}^e \nabla_z \nabla_z E_x^* \right) \rangle, \tag{2.11}$$

where (since $E_z = 0$):

$$Q_{xz}^e = \varepsilon_0 \alpha_{EQ} \frac{\nabla_z E_x^* + \nabla_x E_z^*}{2} = \varepsilon_0 \alpha_{EQ} \frac{\nabla_z E_x^*}{2}. \tag{2.12}$$

As a result, after some trivial math operations, we obtain the following EQ-force:

$$\langle F_z^{EQ} \rangle = -\frac{1}{16} \varepsilon_0 \Re(\alpha_{EQ}) k^3 E_0^2 \sin 2kz. \tag{2.13}$$

To proceed further, one could repeat the same steps to compute the magnetic quadrupole force given as:

$$\langle F_z^{MQ} \rangle = \frac{1}{4} \langle \Re \left(Q_{yz}^m \nabla_z \nabla_z B_y^* \right) \rangle, \tag{2.14}$$

and get the following expression:

$$\langle F_z^{MQ} \rangle = \frac{1}{16} \frac{\Re(\alpha_{MQ})}{\mu_0} k^3 B_0^2 \sin 2kz. \tag{2.15}$$

Overall, the total force formed by the electric and magnetic quadrupoles can be written as:

$$\langle F_z^Q \rangle = \langle F_z^{EQ} \rangle + \langle F_z^{MQ} \rangle = -\frac{1}{16} \varepsilon_0 \Re(\alpha_{EQ}) k^3 E_0^2 \sin 2kz + \frac{1}{16} \frac{\Re(\alpha_{MQ})}{\mu_0} k^3 B_0^2 \sin 2kz. \tag{2.16}$$

2.4 Trapping analysis

Since we have the expressions for the dipole and quadrupole forces derived in the two previous subsections, we can write the total force being equal to:

$$\begin{aligned} \langle F_z \rangle = \langle F_z^D \rangle + \langle F_z^Q \rangle = \frac{1}{8} \varepsilon_0 \Re(\alpha_{ED}) k E_0^2 \sin 2kz - \frac{1}{8} \frac{\Re(\alpha_{MD})}{\mu_0} k B_0^2 \sin 2kz \\ - \frac{1}{16} \varepsilon_0 \Re(\alpha_{EQ}) k^3 E_0^2 \sin 2kz + \frac{1}{16} \frac{\Re(\alpha_{MQ})}{\mu_0} k^3 B_0^2 \sin 2kz. \end{aligned} \tag{2.17}$$

As was mentioned above, we are interested in trapping of a nanoparticle at E-field minimum intensity spot, namely, at $z = 0$. To fulfil the trapping condition, we should have:

$$F_z = -\kappa \cdot z, \kappa > 0, \tag{2.18}$$

where κ is the stiffness of the trap. When $\kappa < 0$, we have anti-trapping case and the total force will take the particle out of the spot $z = 0$. Therefore, given the expression 2.17 for the total force F_z, we can write:

$$\kappa = -\partial_z F_z\big|_{z=0} = -\frac{\varepsilon_0 E_0^2 k^2}{4} \Re \left(\alpha_{ED} - \alpha_{MD} - \frac{1}{2}\alpha_{EQ}k^2 + \frac{1}{2}\alpha_{MQ}k^2 \right). \tag{2.19}$$

It is clearly seen that the sign of the total stiffness κ we get in 2.19 strongly depends on the competition between the Mie-polarizabilities of the corresponding multipole terms. To proceed, we consider a Mie-nanoparticle with radius $R = 150$ nm and refractive index $n = 3.6$. Fig. 2.2 a) shows the absolute values of the Mie-coefficient as a function of the wavelength λ of the standing wave we have. In

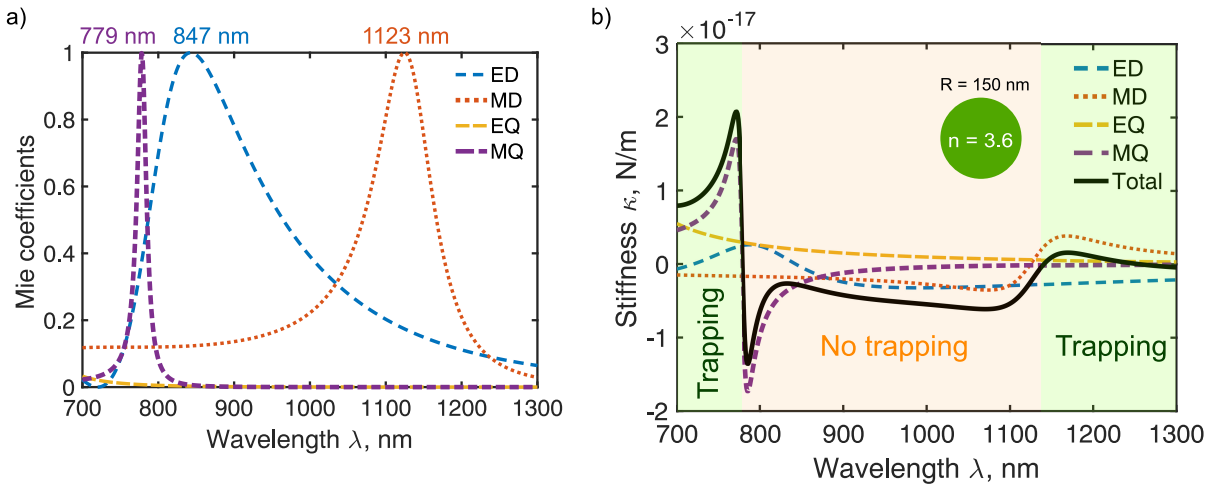

Figure 2.2 — a) Absolute values of Mie-coefficients for electric dipole (ED), magnetic dipole (MD), electric quadrupole (EQ) and magnetic quadrupole (MQ) as a function of the standing wave wavelength λ. b) Total stiffness κ for trapping of a nanoparticle at $z = 0$ position and its decomposition into multipole terms. Green area represents the case when trapping condition ($\kappa > 0$) is full-filled, while orange area defines $\kappa < 0$ - no trapping. Particle parameters: radius $R = 150$ nm, refractive index $n = 3.6$

Fig. 2.1 we plot total stiffness κ defined in 2.19 depending on the trap wavelength λ. It is clearly seen that for $\lambda > 1123$ nm, we have $\kappa > 0$ provided by the MD force (dashed red line) that keeps the particle at $z = 0$. Even though there is a negative contribution from MQ (purple dashed curve) and ED (blue dashed curve) forces, their total contribution seems to be weaker compared to the MD force. If we consider 847 nm $< \lambda < 1123$ nm, there is no trapping since $\kappa < 0$ and the reason is a strong contribution of the electric and magnetic dipole forces taking the particle out of $z = 0$ spot. Stable trapping appears again only when we cross the wavelength of the MQ resonance, that being said, when $\lambda < 779$ nm. Overall, we can make the following statement: if the wavelength of the standing wave is higher than the resonant wavelength of the ED or EQ multipoles, the corresponding forces would take out particle out of $z = 0$, while for the wavelengths lower than the resonant ones, therefore, keeping the particle trapped. Completely opposite effect is provided by the magnetic multipoles. Namely, above the resonant wavelength the corresponding force will keep particle at $z = 0$, as a result, guaranteeing trapping, while below the resonant wavelength it leads to no trapping at all.

To generalize the statement discussed in the paragraph above, we study trap stiffness depending on the particle radius R and the wavelength λ of the standing wave and, as a result, plot the phase map in Fig. 2.3 a) . One can clearly observe that there are regions on the phase map where $\kappa > 0$, therefore, stable trapping is obtained, as well as the cases when $\kappa < 0$ - no trapping. In Fig. 2.3 b) we demonstrate trapping stiffness as a binary phase map, where we define the regions with $\kappa > 0$ (greed areas), provided by the magnetic dipole or magnetic quadrupole forces, respectively.

Finally, we can conclude that a standing wave can be used as a prospective trapping platform for Mie-resonant nanoparticle. By correctly choosing the particle radius as well as the wavelength λ of the standing wave, one can enhance the influence of the magnetic multipoles to achieve stable trapping. At the same time, one can trap a nanoparticle at the node of the magnetic field via the electric dipole and quadrupole forces in a similar way. Since at this particular position the

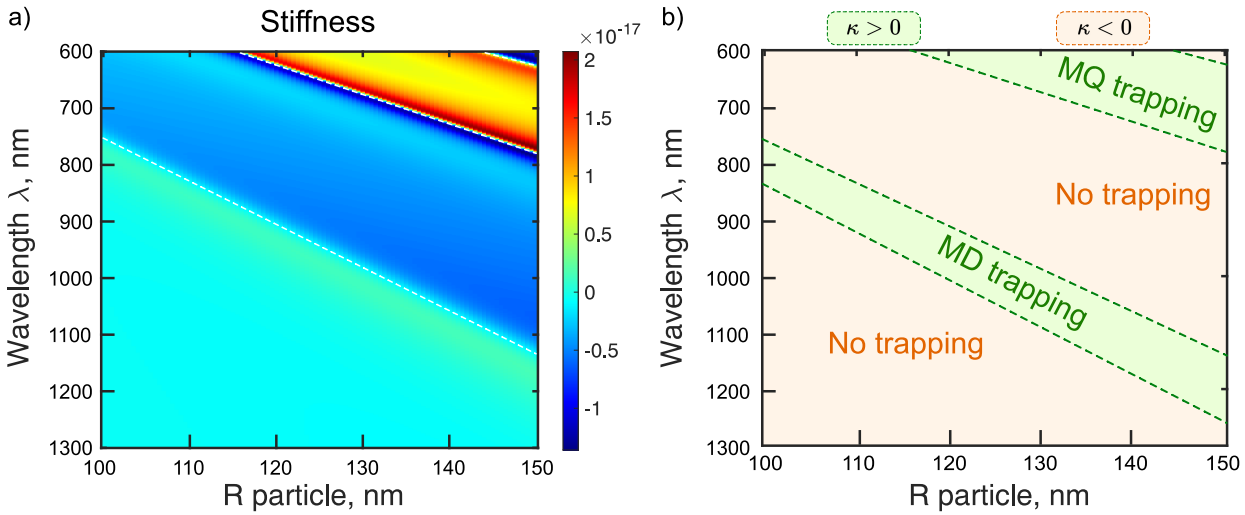

Figure 2.3 — a) Trap stiffness at $z = 0$ as a function of the wavelength λ of the standing wave and particle's radius R. b) Trap stiffness binary map. Green area corresponds to $\kappa > 0$ - trapping, orange area represents $\kappa < 0$ - no trapping. Stable trapping areas for particle radius and wavelength λ are provided by magnetic dipole and quadrupole forces, respectively. Numerical parameters: refractive index $n = 3.6$

electric field intensity achieves its maximum value, one just needs to choose the wavelength to be blue-detuned with respect to the corresponding electric multipole resonances. However, since in the standing wave trap we would always have the strong intensity coming from either electric or magnetic field, the overheating as well as the presence of external noise still exist. Therefore, as we discussed in Introduction, we naturally proceed to the bottle-beam trap and address the possibility of optical trapping at a position where both intensities of electric and magnetic fields can be minimized.

3. BOTTLE-BEAM TRAP

In the following chapter we discuss the bottle-beam trap as a platform to achieve resonant nanoparticle's trapping. We start from the general description of the bottle-beam trap formation. Next, we proceed to the calculation of the force acting on the particle in minimum intensity spot. Finally, we analyse the stiffness behaviour as a function of the beam wavelength and particule's radius to identify configurations when stable trapping can be obtained.

3.1 Trap formation

As was briefly mentioned in Introduction, the bottle-beam trap is formed by the two destructively interfering Gaussian beams. That being said, as illustrated in Fig. 3.1 a), one can consider two beams oriented along z-direction with relative π-phase difference. Next, we focus on axial trapping, therefore, the radial dependency just vanishes, and for further convenience we can assume without loss of generality the electric field to be polarized along x-axis while the magnetic field is oriented along y-direction. As a result, one can rewrite the paraxial approximation of the electric field components for both beams in the following way:

$$\begin{cases} \mathbf{E}_1(z) = E_0\,\hat{\mathbf{e}}_x\,\frac{w_1}{w_1(z)}\exp\left(-i\left(kz-\psi_1(z)\right)\right) \\ \mathbf{E}_2(z) = E_0\,\hat{\mathbf{e}}_x\,\frac{w_2}{w_2(z)}\exp\left(-i\left(\pi+kz-\psi_2(z)\right)\right) \end{cases}, \tag{3.1}$$

as well as the magnetic fields:

$$\begin{cases} \mathbf{B}_1(z) = B_0\,\hat{\mathbf{e}}_y\,\frac{w_1}{w_1(z)}\exp\left(-i\left(kz-\psi_1(z)\right)\right) \\ \mathbf{B}_2(z) = B_0\,\hat{\mathbf{e}}_y\,\frac{w_2}{w_2(z)}\exp\left(-i\left(\pi+kz-\psi_2(z)\right)\right) \end{cases}. \tag{3.2}$$

Finally, the total electric and magnetic fields can be written as:

$$\begin{cases} \mathbf{E}_{\text{total}} = E_0\,\hat{\mathbf{e}}_x\exp\left(-ikz\right)\cdot\left(\frac{w_1}{w_1(z)}e^{i\psi_1(z)}-\frac{w_2}{w_2(z)}e^{i\psi_2(z)}\right) \\ \mathbf{B}_{\text{total}} = B_0\,\hat{\mathbf{e}}_y\exp\left(-ikz\right)\cdot\left(\frac{w_1}{w_1(z)}e^{i\psi_1(z)}-\frac{w_2}{w_2(z)}e^{i\psi_2(z)}\right) \end{cases}. \tag{3.3}$$

Fig. 3.1 b) shows the schematic intensity profile for the electric field in the xz plane. It is worth mentioning that the intensity profile for the magnetic field has the

same structure in the yz-plane. That being said, at the focus center of the Gaussian beams that form the bottle-beam trap we want to achieve minimum intensity. This is the reason why we choose the amplitudes of the electric and magnetic fields to be equal for both beams. As a result, destructive interference between the beams leads to the absence of both electric and magnetic fields, the dark blue dot in Fig. 3.1 b) shows exactly this particular position. At the same time, there are two spots along z-direction with the maximum total intensity (the red points in Fig. 3.1 b)). Finally, the name 'bottle-beam' was mostly motivated by the corresponding intensity profile: according to Fig. 3.1 b), the minimum intensity area (dark-blue region) is surrounded by the higher intensity area (green/yellow regions).

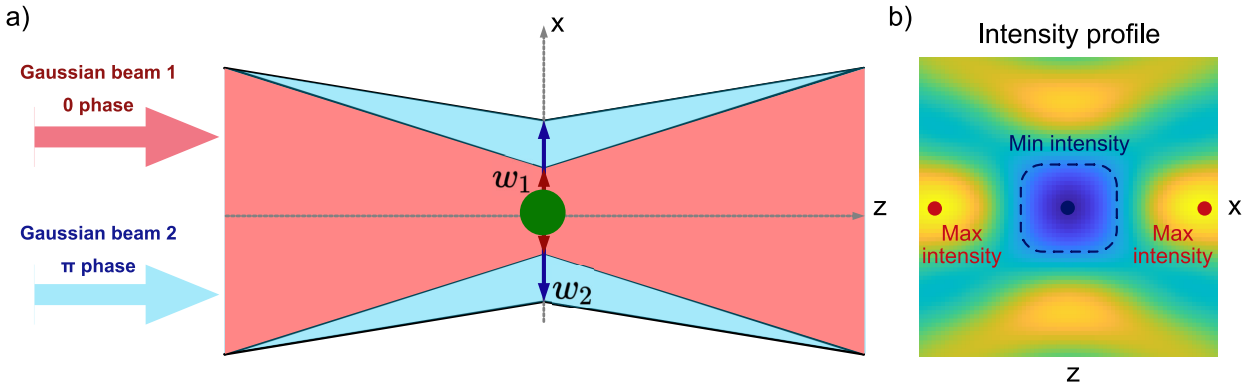

Figure 3.1 — a) Two destructively interfering Gaussian beams oriented along z-direction with π-phase difference. The focus center for both beams is located at $z = 0$, while w_1 and w_2 are the beam waists at the focus spot. b) Intensity profile of the electric field in xz-plane. The dark-blue dot represents the spot with minimum intensity where trapping is desired. The red dots correspond to the maximum intensity spots where conventional trapping is usually observed

Our main goal here is to achieve stable trapping of a resonant nanoparticle in the minimum intensity area. It is worth to highlight one more time the difference between the standing wave and the bottle-beam traps. While for a standing wave one always has the maximum intensity of the magnetic field at the node of the electric field and vice versa, the bottle-beam trap provides a platform where there exists a spot with no electric and magnetic fields at all. In our case, that corresponds to $z = 0$ position.

3.2 Total axial force

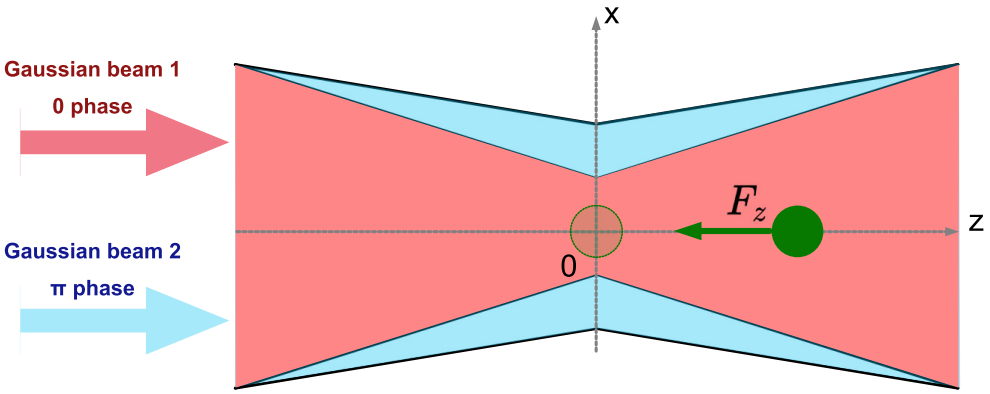

Figure 3.2 — A particle is shifted to the right along z-direction from the focus beam spot at $z = 0$. To provide stable trapping, the total force must point backwards (to the left) towards the equilibrium position. Green transparent area represents stable trapping at minimum intensity spot

Before we address the explicit calculation of the total axial force acting on a resonant nanoparticle placed in the beam focus at $z = 0$, we want to provide an intuitive picture regarding what total axial force profile one could expect along z-direction . First of all, one can imagine the scattering force to be so strong, that there is no trapping at all. In other words, the total force might be completely positive along z such that it always takes the particle out of the trap. The second case is shown in Fig. 3.3 a), where there are two positions at which the total force is zero. To be more precise, the red dot corresponds to the high intensity spot shown in Fig. 3.1 b). At this particular position, trapping is stable, in other words, the associated stiffness κ is positive. However, at the minimum intensity spot, where we actually want to trap the particle, the corresponding stiffness is negative, as a result, trapping is unstable. At the same time, Fig. 3.3 b) shows the last case on how the total force might change along z-axis. In contrast to the case illustrated in Fig. 3.3 a) and discussed above, now the trapping at $z \approx 0$ is stable, that being said, the corresponding stiffness is positive, while the second trapping spot is unstable. Therefore, this is exactly the case we would like to achieve.

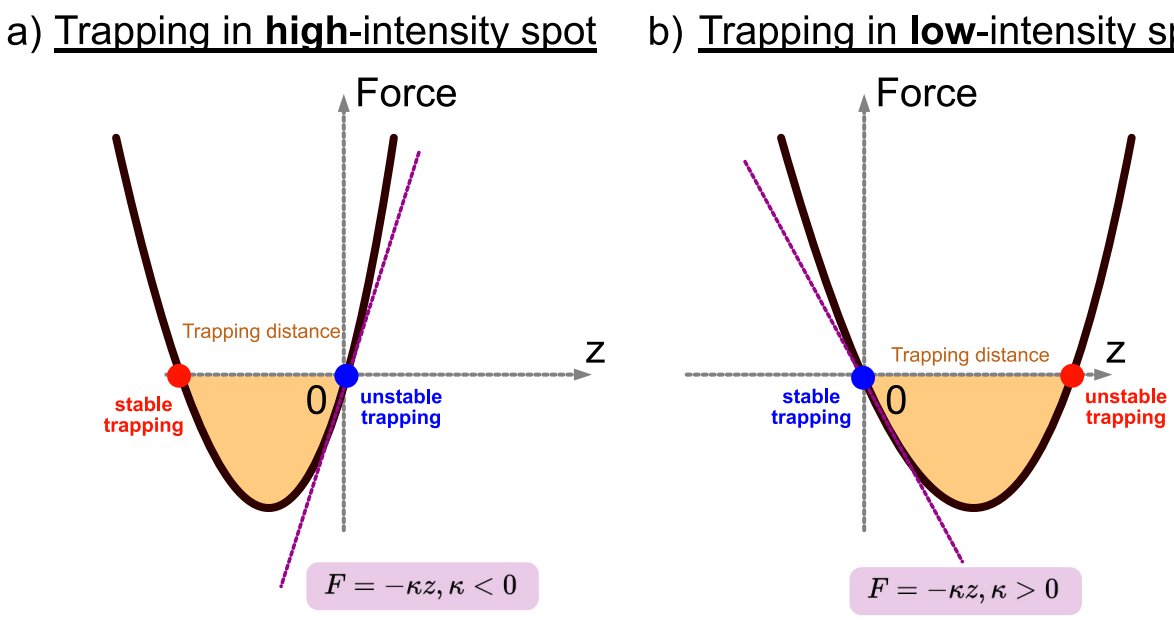

Figure 3.3 — a) Schematic total axial force acting on a nanoparticle when trapping at high intensity spot is observed. The red dot represents the stable trapping out of $z = 0$ position where the total field intensity is minimum. While the blue dot correspond to the unstable trapping since the stiffness κ is negative. b) The total axial force profile when stable trapping at minimum intensity spot is observed, namely, the stiffness $\kappa > 0$

Next, we recall the method presented in Section 1.4 to calculate the total axial force acting on a nanoparticle based on contributions from different multipoles. That being said, we start from the expression of the extinction force as a sum:

$$\langle F_z^{\text{ext}} \rangle = \langle F_z^{ED} \rangle + \langle F_z^{MD} \rangle + \langle F_z^{EQ} \rangle + \langle F_z^{MQ} \rangle, \tag{3.4}$$

where the explicit multipole forces takes the following form:

$$\begin{cases} \langle F_z^{ED} \rangle = \frac{1}{2} \langle \Re \left(p_x \nabla_z E_x^* \right) \rangle \\ \langle F_z^{MD} \rangle = \frac{1}{2} \langle \Re \left(m_y \nabla_z B_y^* \right) \rangle \\ \langle F_z^{EQ} \rangle = \frac{1}{4} \langle \Re \left(Q_{xz}^e \nabla_z^2 E_x^* \right) \rangle \\ \langle F_z^{MQ} \rangle = \frac{1}{4} \langle \Re \left(Q_{yz}^m \nabla_z^2 B_y^* \right) \rangle. \end{cases} \tag{3.5}$$

As one can easily check, according to the system configuration presented in Fig. 3.1, only the terms mentioned above are non-zero.

Following the similar steps, one can calculate the total recoil force as:

$$\langle F_z^{\text{rec}} \rangle = \langle F_z^{ED-EQ} \rangle + \langle F_z^{ED-MQ} \rangle + \langle F_z^{MD-MQ} \rangle + \langle F_z^{EQ-MQ} \rangle, \tag{3.6}$$

where the multipole-multipole force terms can be written as:

$$\begin{cases} \langle F_z^{ED-EQ} \rangle = -\frac{k^4}{12\pi\varepsilon_0 c} \Re \left(p_x m_y^* \right) \\ \langle F_z^{ED-MQ} \rangle = -\frac{k^5}{40\pi\varepsilon_0} \Im \left(Q_{zx}^e p_x^* \right) \\ \langle F_z^{MD-MQ} \rangle = -\frac{k^5}{40\pi\varepsilon_0 c^2} \Im \left(Q_{zy}^e m_y^* \right) \\ \langle F_z^{EQ-MQ} \rangle = -\frac{k^6}{240\pi\varepsilon_0 c} \Re \left(Q_{xz}^e Q_{zy}^{m*} \right). \end{cases} \tag{3.7}$$

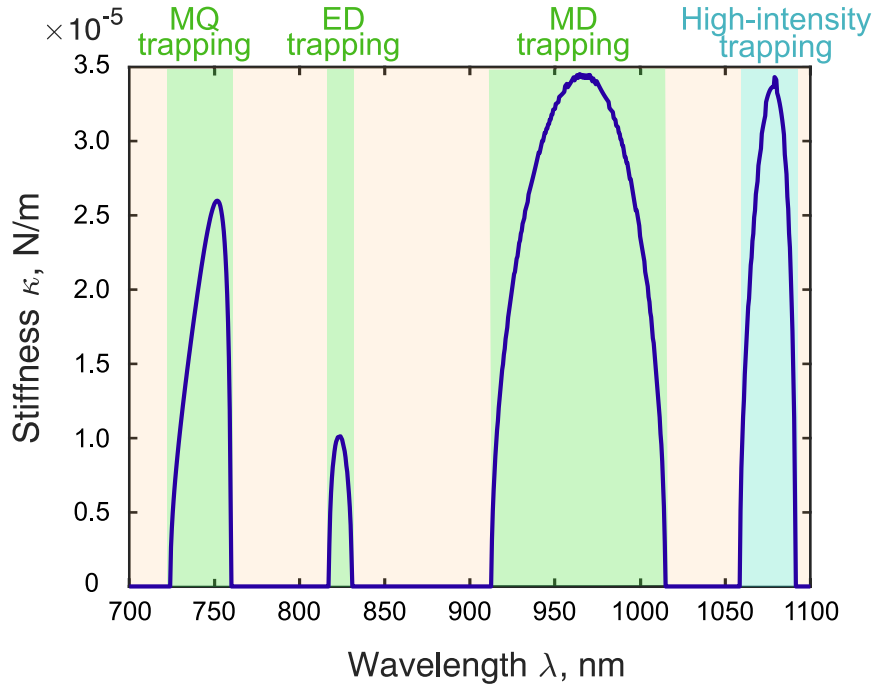

Figure 3.4 — The total axial stiffness κ as a function of the trapping wavelength λ. Green stripes represent stable trapping, $\kappa > 0$, provided by MQ, ED or MD forces, respectively. For orange stripes trapping condition is not fulfilled. Blue range stands for the conventional trapping at maximum intensity spot. Particle parameters: radius $R = 150$ nm, refractive index $n = 3.6$

Based on the expressions presented above, we calculate numerically the total force acting on the nanoparticle. That being said, substituting the electric and magnetic field components of the Gaussian beams, we implement second-order finite-difference scheme to compute the gradient derivatives along z-axis. As a

result, Fig.3.4 shows the trap stiffness κ as a function of the wavelength λ. As always, we are interested only in cases when the stiffness is positive. Therefore, the green areas in Fig.3.4 identify the particular ranges of λ when stable trapping at minimum intensity spot can be obtained. The orange areas represents the cases when there is no trapping at all due to the strong scattering force. Moreover, the multipole analysis we implement allows to classify a pacrticular multipole that contribute the most instable trapping formation. To be more precise, for 725 nm $< \lambda < 760$ nm trapping is provided by MQ force, for 820 nm $< \lambda < 830$ nm - by ED force, for 915 nm $< \lambda < 1020$ nm - by MD force. The blue range of the wavelength λ corresponds to the conventional high-intensity spot trapping illustrated in Fig. 3.3 a).

3.3 Axial trapping analysis

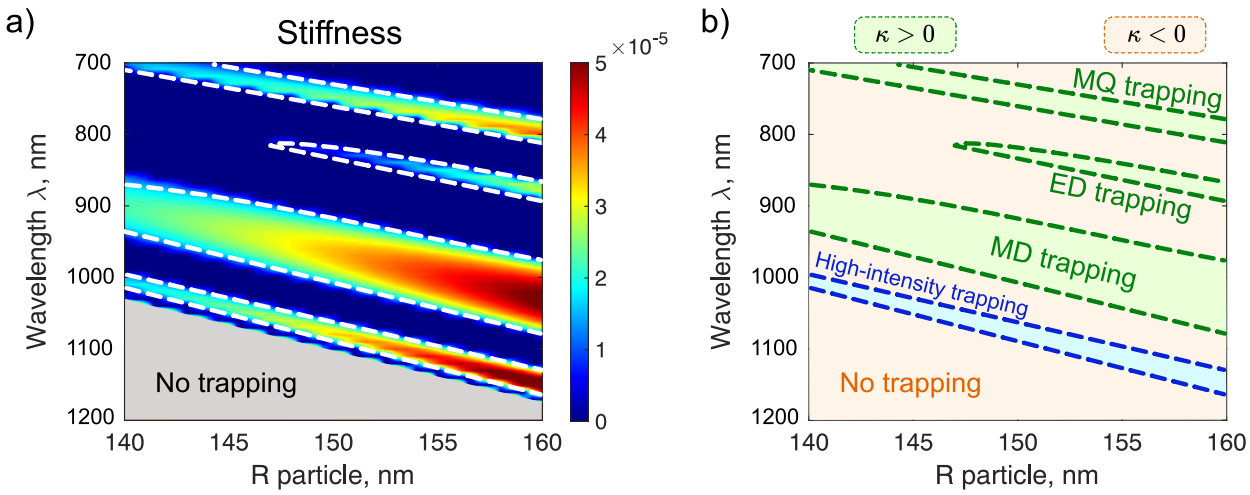

Figure 3.5 — a) Total axial stiffness depending on the beam wavelength λ and on the particle's radius R. The grey area corresponds to the case when there is no trapping due to the strong contribution of the scattering force. b) Axial stiffness binary map. Green areas represent $\kappa > 0$ provided by the MD, ED and EQ forces, respectively. Blue area correspond to high-intensity trapping. Particle parameters: refractive index $n = 3.6$

Next, we study the trap stiffness as we did for the standing wave trap above. Namely, Fig. 3.5 a) shows the axial stiffness κ as a function of the Gaussian beams' wavelength λ and particle's radius R. To plot this 2D map, we proceed as follows:

at first, we distinguish the case when there is no trapping at all since the scattered force is dominating, as a result, the grey area in Fig. 3.5 a) directly represents this particular case. Next, we select configurations when the stiffness κ is negative, in other words, when trapping is unstable, and represent it via the dark blue areas in Fig. 3.5 a). And the only case left is exactly the one we are interested in, namely, when stable trapping is achieved at a position close to the focus beam center $z = 0$. That being said, Fig. 3.5 b) shows when low-intensity trapping is observed and the main multipole that contributes to each particular trapping. In addition, we are also able to identify conventional trapping at the maximum intensity spot.

3.4 Total transverse force

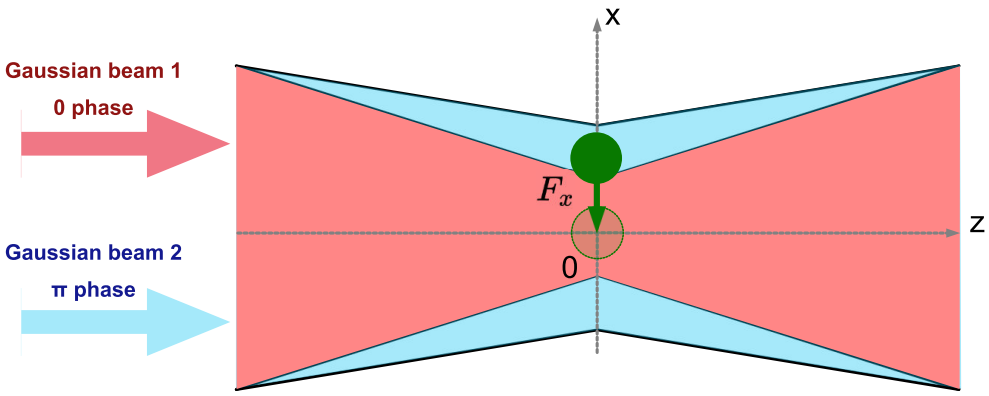

Figure 3.6 — A particle is shifted along x-direction in the bottle-beam trap above the equilibrium position at $x = y = z = 0$. To achieve stable trapping, the total transverse optical force F_x must point down to the equilibrium spot. For displacement below the trapping spot, the force direction should be the opposite

Since in the previous section we discuss the axial force acting on a nanoparticle, now we proceed to radial trapping. Without loss of generality and taking into account the axial symmetry of the bottle-beam trap, we consider the transverse force acting on a nanoparticle shifted along x-direction as illustrated in Fig. 3.6. Therefore, we are interested whether it is possible to obtain the total transverse force that keeps the particle at minimum intensity spot.

In this case, we can assume $y = z = 0$, as a result, the electric field components of two Gaussian beams are simplified into:

$$\begin{cases} E_x^1(x) = E_0 \cdot e^{-\frac{x^2}{w_1^2}} \\ E_x^2(x) = -E_0 \cdot e^{-\frac{x^2}{w_2^2}} \end{cases}, \tag{3.8}$$

where indices $(1,2)$ represents the first and the second beams, respectively. At the same time, the magnetic field components can be written as:

$$\begin{cases} B_y^1(x) = B_0 \cdot e^{-\frac{x^2}{w_1^2}} \\ B_y^2(x) = -B_0 \cdot e^{-\frac{x^2}{w_2^2}} \end{cases}, \tag{3.9}$$

where the "$-$"sign shows the π-phase difference between the beams. As a result, the total field components are the following:

$$\begin{cases} E_x^{\text{total}}(x) = E_0 \cdot \left(e^{-\frac{x^2}{w_1^2}} - e^{-\frac{x^2}{w_2^2}} \right) \\ B_y^{\text{total}}(x) = B_0 \cdot \left(e^{-\frac{x^2}{w_1^2}} - e^{-\frac{x^2}{w_2^2}} \right) \end{cases}. \tag{3.10}$$

Next, we proceed to the transverse force calculation. First of all, for radially shifted nanoparticle the scattering force is zero. This statement can be understood in two ways: by direct calculation observing that the corresponding real and imaginary parts vanish, or by the fact that scattering force is proportional to the Poynting vector that is equal to zero for the decaying EM fields presented in 3.10. As a result, the total force acting on the nanoparticle can be represented as a sum of the gradient forces associated with the set of multipoles in the following way:

$$\langle F_x \rangle = \langle F_x^{ED} \rangle + \langle F_x^{MD} \rangle + \langle F_x^{EQ} \rangle + \langle F_x^{MQ} \rangle, \tag{3.11}$$

where the multipole forces can be written as:

$$\begin{cases} \langle F_x^{ED} \rangle = \frac{\varepsilon_0}{2} \langle \Re \left(\alpha_{ED} E_x^{\text{total}} \nabla_x E_x^{\text{total}} \right) \rangle \\ \langle F_x^{MD} \rangle = \frac{1}{2\mu_0} \langle \Re \left(\alpha_{MD} B_y^{\text{total}} \nabla_x B_y^{\text{total}} \right) \rangle \\ \langle F_x^{EQ} \rangle = \frac{\varepsilon_0}{4} \langle \Re \left(\alpha_{EQ} \nabla_x E_x^{\text{total}} \nabla_x^2 E_x^{\text{total}} \right) \rangle \\ \langle F_x^{MQ} \rangle = \frac{1}{4\mu_0} \langle \Re \left(\alpha_{MQ} \nabla_x B_y^{\text{total}} \nabla_x^2 B_y^{\text{total}} \right) \rangle \end{cases}. \tag{3.12}$$

Here, in contrast to axial trapping discussed above, the gradient derivatives are taken with respect to x, as a result, only x component of the total force is non-zero.

To proceed further, we calculate the stiffness κ at $x \approx 0$ by expanding the force components presented in 3.12 in Taylor series and taking into account only linear terms with respect to x. As a result, we get the following approximation for κ:

$$\kappa\big|_{x=0} \approx \left(1/w_2^2 - 1/w_1^2\right)^2 \cdot \left(\varepsilon_0 E_0^2 \Re\left(\alpha_{EQ}\right) + \frac{1}{\mu_0} B_0^2 \Re\left(\alpha_{MQ}\right)\right). \tag{3.13}$$

One can clearly notice that only quadrupole terms contribute to the stiffness in this case. It can be also seen in 3.12, where, since $E_x^{\text{total}} = B_y^{\text{total}} = 0$ at the beam focus center. Next, similarly to the standing wave trap we observe the competition between different multipole forces, to be more precise, related to electric and magnetic quadrupoles. As we already discussed, the fact whether EQ or MQ force will keep the particle at the focus spot or take it away from the equilibrium position strongly depends on the wavelength of the trapped beams. That being said, this dependency is contained in the Mie polarizabilities α_{EQ} and α_{MQ}, thus, below we analyse the transverse stiffness in more detail.

Fig. 3.7 b) shows the transverse stiffness κ depending on the wavelength λ. As before, the green areas represent the cases when stable trapping is observed, in other words, when the stiffness is positive, while the orange regions state for $\kappa < 0$, the absence of trapping. By comparing Fig. 3.7 b) with Fig. 3.7 a) where the absolute value of Mie-coefficients are plotted, one can clearly see that for 580 nm $< \lambda <$ 625 nm transverse trapping is achieved by the EQ force, while for 755 nm $< \lambda <$ 779 nm stable trapping is provided by the MQ force. Therefore, here one can notice the similar effect we observe for the standing wave trap, namely, by choosing the wavelength λ from the corresponding side of the multipole resonance (in this particular case, of EQ or MQ resonance), we can observe trapping in minimum intensity spot.

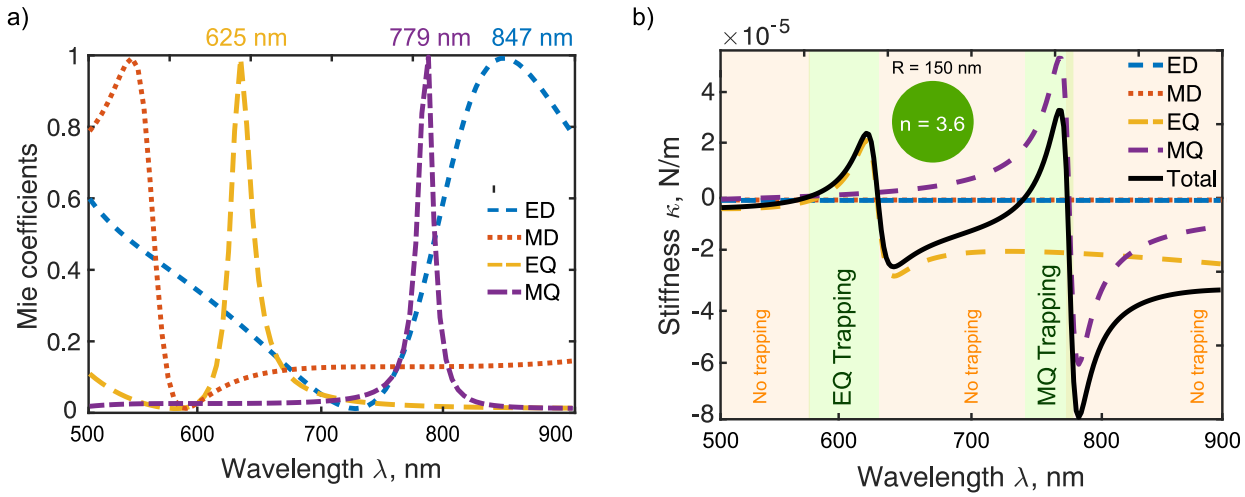

Figure 3.7 — a) Absolute values of Mie-coefficients for electric dipole (ED), magnetic dipole (MD), electric quadrupole (EQ) and magnetic quadrupole (MQ) as a function of the standing wave wavelength λ. b) Transverse stiffness κ for trapping of a nanoparticle at $z = 0$ position and its decomposition into multipole terms. Green stripes represent the case when stable trapping ($\kappa > 0$) is achieved , while orange stripes defines $\kappa < 0$ - no trapping. Particle parameters: refractive index $n = 3.6$

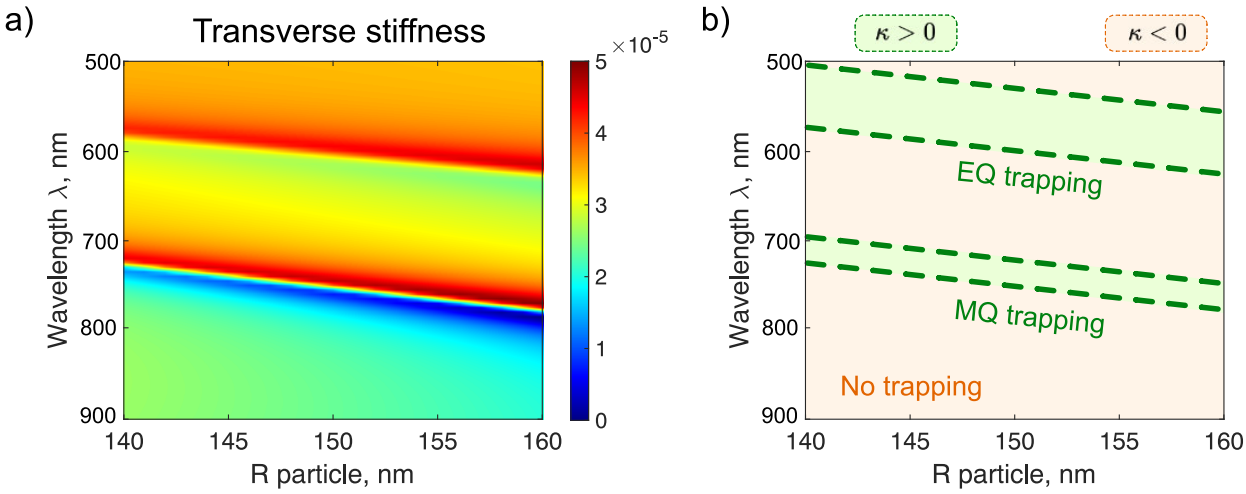

Figure 3.8 — a) Transverse stiffness as a function of λ and particle's radius R. b) Transverse stiffness phase map. Green areas $\kappa > 0$ represent stable trapping provided by MQ and EQ forces, respectively. Particle parameters: refractive index $n = 3.6$

3.5 Transverse trapping analysis

Now we want to investigate transverse trap stiffness as usually in this thesis depending on the wavelenght λ and R-radius of the particle. Fig. 3.8 a)

shows the transverse stiffness map, where one can notice two areas of parameter configurations with $\kappa > 0$. To be more precise, Fig. 3.8 b) shows directly the ranges of λ and R when stable trapping can be obtained. As before, the multipole approach we implement allow as to identify that trapping is achieved due to the MQ or EQ forces, respectively, in agreement with the expression derived in 3.13.

To summarize the results presented in this chapter, we observe that the bottle-beam trap can be used to achieve stable trapping in minimum intensity spot. The multipole decomposition method allows to define the ranges of the particle's radius R and beam wavelength λ such that the total axial or transversal stiffnesses are positive. If one compare the binary phase maps for axial (see Fig. 3.7a)) and transverse (see Fig. 3.8 b)) stiffnesses, we see that the particular green area associated with the MQ trapping force provides trapping in all desired directions, in other words, both for axial and radial trappings. At the same time, MD trapping is achieved for displacements along z-direction, while there is no transverse trapping in the corresponding ranges of λ and R.

4. OPTICAL TORQUE INDUCED BY THE SECOND HARMONIC GENERATION

As was announced in Introduction, resonant nanoparticles provide new opportunities not only for optical trapping, but also for optomechanical manipulations. In the following chapter, we address the rotation properties, and propose a novel mechanism to achieve the angular-momentum transfer to a non-absorbing particle induced by the second harmonic generation. That being said, the mechanism we introduce is completely different compared to earlier well-known ways to optically rotate a particle based on either the rotational symmetry breaking or on the presence of particle's absorption.

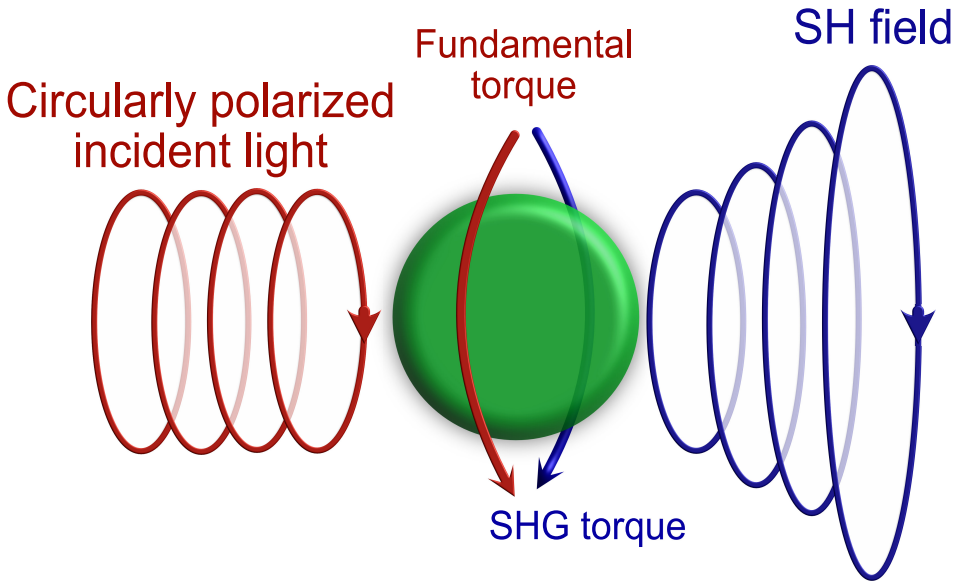

Figure 4.1 — A spherical nanoparticle illuminated by circularly polarized light at the frequency ω generates scattered second-harmonic field at the doubled frequency. Total torque acting on the nanoparticle is a sum of the torque induced by incident light (fundamental torque) and torque associated with the scattered SH field (SH torque)

To be more precise, we consider a spherical nanoparticle illuminated by circularly polarised incident light as illustrated in Fig. 4.1. We assume the emergence of the second harmonic scattered field, as a result, total torque $\mathbf{T}^{\text{total}}$ acting on the nanoparticle can be written, in general, as a sum of fundamental

torque $\mathbf{T}^{(\omega)}$ coming from the incident light and torque $\mathbf{T}^{(2\omega)}$ generated by the second harmonic scattered field. Therefore, below we present explicit derivations for the mentioned torque components based on the multipole decomposition.

4.1 VSH approach for optical torques

In the following subsection we discuss the approach to calculate optical torque acting on a nanoparticle using complex vector spherical harmonics (VSH) as a main tool we used for our work. First of all, we start form the general expression for time-averaged torque mentioned in [40; 41]:

$$\mathbf{T} = \oint_S \hat{M} \cdot \mathbf{n} dS, \tag{4.1}$$

where $\mathbf{n}$ stands for outer unit normal vector to the surface S, while $\hat{M} = \mathbf{r} \times \hat{\mathcal{T}}$ represents the angular momentum flux tensor. $\hat{\mathcal{T}}$ corresponds to the Maxwell's stress tensor defined as:

$$\hat{\mathcal{T}} = \frac{1}{2}\Re\left(\varepsilon\varepsilon_0 \mathbf{E}^* \otimes \mathbf{E} + \mu\mu_0 \mathbf{H}^* \otimes \mathbf{H} - \frac{1}{2}\left(\varepsilon\varepsilon_0 |\mathbf{E}|^2 + \mu\mu_0 |\mathbf{H}|^2\right)\hat{\mathcal{I}}\right). \tag{4.2}$$

For further convenience, one can choose the integration surface to be just a perfect sphere and simplify the integral 4.1 into [42; 43]:

$$\mathbf{T} = -\frac{r^3}{2}\Re \int_{4\pi} d\Omega \Big(\left(\varepsilon\varepsilon_0 E_r^* E_\varphi + \mu\mu_0 H_r^* H_\varphi\right)\hat{\mathbf{e}}_\vartheta - \left(\varepsilon\varepsilon_0 E_r^* E_\vartheta + \mu\mu_0 H_r^* H_\vartheta\right)\hat{\mathbf{e}}_\varphi \Big), \tag{4.3}$$

where the integration is performed over the solid angle $d\Omega$, and the electric and magnetic field components are represented in spherical coordinates (r, θ, φ).

Next, we use VSH to represent the electric and magnetic fields in the following way [34]:

$$\begin{cases} \mathbf{E} = \sum\limits_{n=1}^{\infty} \sum\limits_{m=-n}^{n} \left(A_{mn}\mathbf{M}_{mn} + B_{mn}\mathbf{N}_{mn}\right) \\ \mathbf{H} = \frac{1}{iZ} \sum\limits_{n=1}^{\infty} \sum\limits_{m=-n}^{n} \left(A_{mn}\mathbf{N}_{mn} + B_{mn}\mathbf{M}_{mn}\right), \end{cases} \tag{4.4}$$

Here Z represents the total medium impedance, $\mathbf{M}_{mn}$ and $\mathbf{N}_{mn}$ stand for the magnetic and electric multipoles, respectively, with the total angular momentum n and the z-projection of the total angular momentum being equal to m.

The total fields are formed by the incident and scattered ones, namely, $\mathbf{E} = \mathbf{E}^{\text{inc}} + \mathbf{E}^{\text{scat}}$ and $\mathbf{H} = \mathbf{H}^{\text{inc}} + \mathbf{H}^{\text{scat}}$. Thus, we can use the VSH notation presented above and express the incident and scattered fields as [34]:

$$\begin{cases} \mathbf{E}^{\text{inc}} = \sum\limits_{n=1}^{\infty} \sum\limits_{m=-n}^{n} (A_{mn}^{\text{inc}} \mathbf{M}_{mn}^{(1)} + B_{mn}^{\text{inc}} \mathbf{N}_{mn}^{(1)}) \\ \mathbf{E}^{\text{scat}} = \sum\limits_{n=1}^{\infty} \sum\limits_{m=-n}^{n} (A_{mn}^{\text{scat}} \mathbf{M}_{mn}^{(3)} + B_{mn}^{\text{scat}} \mathbf{N}_{mn}^{(3)}) \end{cases}, \tag{4.5}$$

as well as

$$\begin{cases} \mathbf{H}^{\text{inc}} = \frac{1}{iZ} \sum\limits_{n=1}^{\infty} \sum\limits_{m=-n}^{n} (A_{mn}^{\text{inc}} \mathbf{N}_{mn}^{(1)} + B_{mn}^{\text{inc}} \mathbf{M}_{mn}^{(1)}) \\ \mathbf{H}^{\text{scat}} = \frac{1}{iZ} \sum\limits_{n=1}^{\infty} \sum\limits_{m=-n}^{n} (A_{mn}^{\text{scat}} \mathbf{N}_{mn}^{(3)} + B_{mn}^{\text{scat}} \mathbf{M}_{mn}^{(3)}). \end{cases} \tag{4.6}$$

Finally, performing the integration presented in 4.3 and taking into account the orthogonality properties for VSH [44; 45], we obtain the following expression for the torque component along z-direction:

$$T_z = T_z^{\text{amp}} + T_z^{\text{cross}}, \tag{4.7}$$

where T_z^{amp} associated with the amplitudes of expansion coefficients and equal to:

$$T_z^{\text{amp}} = -\frac{\varepsilon\varepsilon_0}{2k(\omega)^3} \sum_{n=1}^{\infty} \sum_{m=-n}^{n} mn(n+1) \left(|A_{mn}^{\text{scat}}|^2 + |B_{mn}^{\text{scat}}|^2 \right), \tag{4.8}$$

while T_z^{cross} contains the interference terms between incident and scattered fields as:

$$T_z^{\text{cross}} = -\frac{\varepsilon\varepsilon_0}{2k(\omega)^3} \sum_{n=1}^{\infty} \sum_{m=-n}^{n} mn(n+1) Re \left(A_{mj}^{\text{inc}} A_{mn}^{\text{scat}*} + B_{mn}^{\text{inc}} B_{mn}^{\text{scat}*} \right). \tag{4.9}$$

4.2 Torque on the fundamental frequency

As was mentioned above, we consider circularly polarised incident light and, without loss of generality, magnetic number m_{i} is equal to $+1$ for right-hand

polarization. As a result, the VSH coefficients related to the incident field take the following form [34]:

$$\begin{cases} A_{mn}^{\text{inc}} \sim \sqrt{\frac{4\pi(2n+1)}{n(n+1)}} \cdot \delta_{m,m_{\text{i}}} \\ B_{mn}^{\text{inc}} = m_{\text{i}} \cdot A_{mn}^{\text{inc}}. \end{cases} \tag{4.10}$$

Next, VSH coefficients related to the scattered fields are proportional to the Mie-scattering coefficients a_n and b_n [34], as a result, equal to:

$$\begin{cases} A_{mn}^{\text{scat}} \sim a_n \cdot \delta_{m,m_{\text{i}}} \\ B_{mn}^{\text{scat}} \sim b_n \cdot \delta_{m,m_{\text{i}}}. \end{cases} \tag{4.11}$$

Finally, substituting 4.10 and 4.11 into 4.9, we get $T_z^{(\omega)}$ to be proportional to the absorption cross-section, namely:

$$\sigma_{\text{abs}} \sim T_z^{(\omega)} = \sum_{n=1}^{\infty} n(n+1) \left(Re(a_n + b_n) - (|a_n|^2 + |b_n|^2) \right), \tag{4.12}$$

and, to be more precise, take the following form:

$$T_z^{(\omega)} = \frac{c}{n_m} \cdot \sigma_{\text{abs}} S_z^{(\omega)}, \tag{4.13}$$

where n_m represents the refractive index of medium, σ_{abs} is the absorption cross-section, $S_z^{(\omega)} = \frac{m_{\text{i}}}{2\omega} \varepsilon \varepsilon_0 E_0^2$ stands for z-component of the canonical spin-angular momentum density.

Next, we assume that all the absorbed power coming from the incident light goes directly to the second harmonic generation. In other words, we have $\sigma_{\text{abs}} \rightarrow \sigma_{\text{SHG}}$, where σ_{SHG} represents the SHG cross-section. As a result, the expression for the fundamental torque can be re-written as:

$$T_z^{(\omega)} = \frac{c}{n_m} \cdot \sigma_{\text{SHG}} S_z^{(\omega)}. \tag{4.14}$$

To compute σ_{SHG}, we follow the approach presented in [46]. At first, one can represent the scattered second harmonic field via real VSH in the following way:

$$\mathbf{E}^{2\omega}(\mathbf{r}) = \sum_{n=1}^{\infty} \sum_{m=0}^{n} \sum_{W=M,N} \left(D_{Wemj} \mathbf{W}_{emj}^{(3)} \left(k_1(2\omega), \mathbf{r} \right) + D_{Womj} \mathbf{W}_{omj}^{(3)} \left(k_1(2\omega), \mathbf{r} \right) \right), \tag{4.15}$$

where $k_1(2\omega) = \frac{\sqrt{\varepsilon_1}\cdot 2\omega}{c}$ represents the wave vector of the outside medium, $\mathbf{W} = \mathbf{M}, \mathbf{N}$ stand for the electric and magnetic real vector spherical harmonics such that the superscript (3) corresponds to the first-kind spherical Hankel functions , while (1) states for the first-kind spherical Bessel function [34]. $D_{W_{e}^{o}mn}$ are the expansion coefficients that, according to [46], are proportional to:

$$D_{W_{\substack{e\\o}mj}} \sim \int_V \mathbf{W}^{(1)}_{\substack{e\\o}mn}(k_2(2\omega), \mathbf{r}) \cdot \mathbf{P}^{2\omega}(\mathbf{r}) dV, \tag{4.16}$$

where $\mathbf{P}^{2\omega}(\mathbf{r})$ states for the nonlinear polarization at the second-harmonic frequency and defined via the second-order polarizability tensor $\hat{\chi}$ as:

$$\mathbf{P}^{2\omega}(\mathbf{r}) = \hat{\chi}\mathbf{E}^{(\omega)}(\mathbf{r})\mathbf{E}^{(\omega)}(\mathbf{r}), \tag{4.17}$$

and $k_2(2\omega) = \frac{\sqrt{\varepsilon_2}\cdot 2\omega}{c}$ represents the wave vector inside the particle.

At the same time, we can express the scattered field via the complex VSH as [46]:

$$\mathbf{E}^{2\omega}(\mathbf{r}) = \sum_{n=1}^{\infty}\sum_{m=-n}^{n}\left(a_{mn}^{\text{scat}}\mathbf{M}_{mn}^{(3)} + b_{mn}^{\text{scat}}\mathbf{N}_{mn}^{(3)}\right). \tag{4.18}$$

To connect the expansion coefficients $D_{W_{e}^{o}mn}$ related to the real VSH with $a_{mn}^{\text{scat}}, b_{mn}^{\text{scat}}$ coming from the complex VSH decomposition, one can use the following relation between real and complex VSH for non-negative $m \geqslant 0$ presented in [34]:

$$\mathbf{W}_{mn} = \sqrt{\frac{2n+1}{4\pi}\frac{(n-m)!}{(n+m)!}}\left(\mathbf{W}_{emn} + i\mathbf{W}_{omn}\right) = \beta_{mn}\left(\mathbf{W}_{emn} + i\mathbf{W}_{omn}\right), \tag{4.19}$$

where $\beta_{mn} = \sqrt{\frac{2n+1}{4\pi}\frac{(n-m)!}{(n+m)!}}$. Next, in order to generalize this relation for negative m, we use the following symmetry property for $m \geqslant 0$:

$$\mathbf{W}_{-mn} = (-1)^m\mathbf{W}^*_{mn} = (-1)^m\beta_{mn}\left(\mathbf{W}_{emn} - i\mathbf{W}_{omn}\right). \tag{4.20}$$

As a result, we can convert the expansion coefficients from real VSH to complex ones and vice versa as follows:

$$m > 0: \begin{cases} a_{mn}^{\text{scat}} = \dfrac{D_{Memn}}{2\beta_{mn}} + \dfrac{D_{Momn}}{2i\beta_{mn}} \\ b_{mn}^{\text{scat}} = \dfrac{D_{Nemn}}{2\beta_{mn}} + \dfrac{D_{Nomn}}{2i\beta_{mn}} \end{cases},$$

$$m=0:\begin{cases} a^s_{mn}=\dfrac{D_{Memn}}{2\beta_{mn}} \\ b^s_{mn}=\dfrac{D_{Nemn}}{2\beta_{mn}} \end{cases},$$

$$m<0:\begin{cases} a^s_{mn}=\dfrac{(-1)^{|m|}D_{Me|m|n}}{2\beta_{|m|n}}-\dfrac{(-1)^{|m|}D_{Mo|m|n}}{2i\beta_{|m|n}} \\ b^s_{mn}=\dfrac{(-1)^{|m|}D_{Ne|m|n}}{2\beta_{|m|n}}-\dfrac{(-1)^{|m|}D_{No|m|n}}{2i\beta_{|m|n}} \end{cases}. \tag{4.21}$$

Finally, one can use the relations presented above together with the expression of the SHG cross-section defined via the real VSH expansion coefficients as [46]:

$$\begin{aligned} \sigma_{\text{SHG}} &= \frac{2\pi}{k_1(2\omega)^2}\sum_{n=1}^{\infty}\sum_{W=M,N}\frac{n(n+1)}{(2n+1)}\times \\ &\times\left(\sum_{m=1}^{n}\frac{(n+m)!}{(n-m)!}\left(|D_{Wemn}|^2+|D_{Womn}|^2\right)+2\,|D_{We0n}|^2\right) \end{aligned} \tag{4.22}$$

to rewrite the fundamental torque 4.14 in the following way:

$$T_z^{(\omega)}=m_{\text{i}}T_0\frac{\sigma_{\text{SHG}}}{\sigma_{\text{geom}}}=m_{\text{i}}T_0\frac{1}{\sigma_{\text{geom}}}\frac{1}{k(2\omega)^2}\sum_{n=1}^{\infty}\sum_{m=-n}^{n}\left(W^{\text{E}}_{mn}+W^{\text{M}}_{mn}\right). \tag{4.23}$$

Here $\sigma_{\text{geom}}=\pi a^2$ is the geometrical cross section, $T_0=\frac{\varepsilon\varepsilon_0}{2k(\omega)}E_0^2\sigma_{\text{geom}}$ is a normalization factor. W^{E}_{mn} and W^{M}_{mn} are the dimensionless expansion coefficients related to a^{scat}_{mn} and b^{scat}_{mn} in the following way:

$$\begin{cases} W^{\text{E}}_{mn}=\frac{n(n+1)}{E_0^2}\left|a^{\text{scat}}_{mn}\right|^2 \\ W^{\text{M}}_{mn}=\frac{n(n+1)}{E_0^2}\left|b^{\text{scat}}_{mn}\right|^2. \end{cases} \tag{4.24}$$

4.3 Torque on the doubled frequency

Next, we want to compute the torque associated with the doubled frequency 2ω. Taking into account the fact that there is no incident field at this particular frequency, the corresponding VSH expansion coefficients $A^{\text{inc}}_{mn}=B^{\text{inc}}_{mn}=0$. As a result, only scattering coefficients A^{scat}_{mn} and B^{scat}_{mn} are non-zero. Therefore, recalling the general expression of the torque derived in 4.9, we get the following

SH torque where only squared amplitudes associated with expansion coefficients of the scattered fields are involved :

$$T_z^{(2\omega)} = -\frac{\varepsilon\varepsilon_0}{2k(\omega)^3}\sum_{n=1}^{\infty}\sum_{m=-n}^{n} mn(n+1)\left(|A_{mn}^{\text{scat}}|^2 + |B_{mn}^{\text{scat}}|^2\right). \tag{4.25}$$

To proceed further, we use the dimensionless expansion coefficients we introduced above, and the SH torque can be re-written as:

$$T_z^{(2\omega)} = -\frac{1}{2}T_0\frac{1}{\sigma_{\text{geom}}}\sum_{n=1}^{\infty}\sum_{m=-n}^{n} m\left(W_{mn}^{\text{E}} + W_{mn}^{\text{M}}\right), \tag{4.26}$$

where, as we did for the fundamental torque, the normalization factor T_0 was used.

4.4 Total torque

Finally, since we obtain the expressions for torques on the fundamental and double frequencies, total torque acting on a nanoparticle takes the following form:

$$T_z^{\text{total}} = T_z^{(\omega)} + T_z^{(2\omega)} = \frac{1}{2}T_0\frac{1}{\sigma_{\text{geom}}k(2\omega)^2}\sum_{nm}(2m_{\text{inc}} - m)\left(W_{mn}^{\text{E}} + W_{mn}^{\text{M}}\right). \tag{4.27}$$

As a result, given the dimensionless expansion coefficients W_{mn}^{E} and W_{mn}^{M}, one can directly compute total torque. Since it is impossible to calculate these coefficients fully analytically, we address the numerical approach. To be more precise, we compute overlapping integrals presented in 4.16 to obtain the real VSH expansion coefficients $D_{W_e^o mn}$. Next, we use the relation between real and complex expansion coefficients 4.21 to convert numerically $D_{W_e^o mn}$ into a_{mn}^s, b_{mn}^s. Therefore, we can use 4.24 to calculate $W_{mn}^{\text{E}}, W_{mn}^{\text{M}}$, and, finally, compute the total torque acting on a nanoparticle. Below we illustrate the emergence of non-linear induced torque for a concrete example.

That being said, we consider a spherical nanoparticle made of GaAs as one of the most-common materials to observe the second harmonic generation in real experiments [47]. The wavelength of the incident light is $\lambda = 1550$ nm, while the refractive indices at the frequencies ω and 2ω are slightly different, and equal to

$n^{\omega} = 3.28$ and $n^{2\omega} = 3.58$, respectively. In the principal axes the only non-zero components of the second-order susceptibility tensor $\chi^{(2)}_{\text{GaAs}}$ are the following:

$$\chi^{(2)}_{xyz} = \chi^{(2)}_{yzx} = \chi^{(2)}_{zxy} = \chi^{(2)}_{xzy} = \chi^{(2)}_{zyx} = \chi^{(2)}_{yxz} = \chi^{(2)}_{\text{GaAs}} = 100 \text{ pm/V}. \tag{4.28}$$

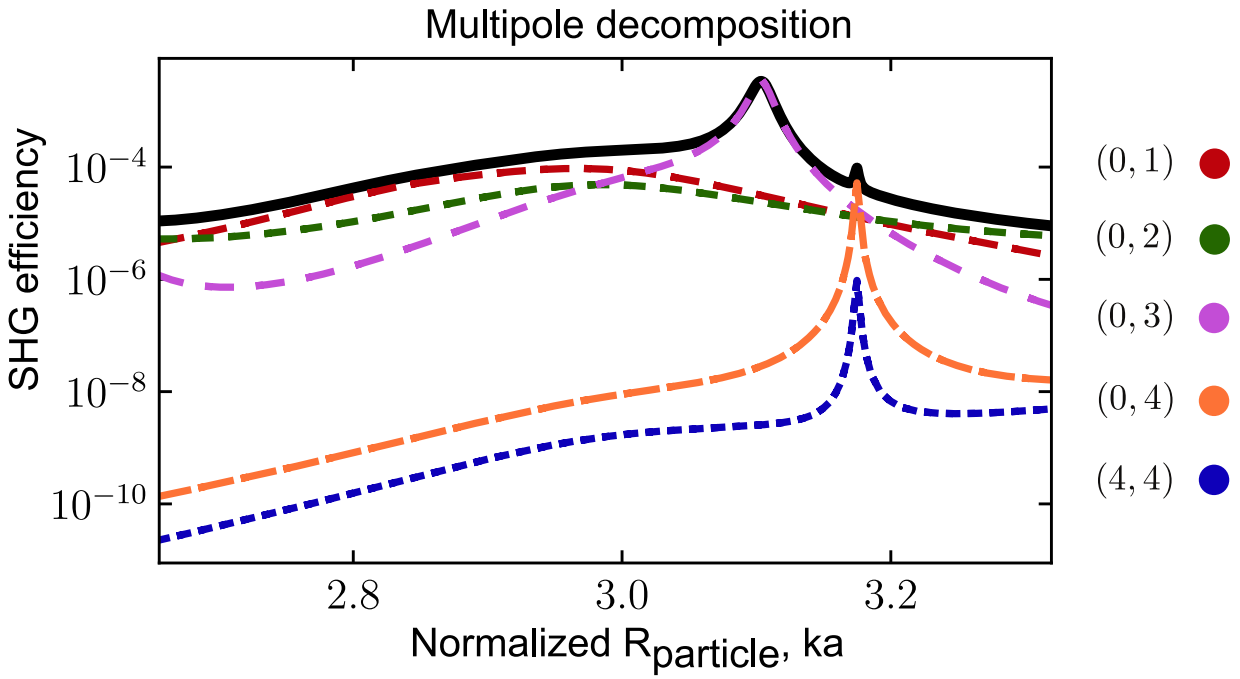

Figure 4.2 — SHG efficiency produced by a spherical GaAs nanoparticle depending on its normalized radius. The dashed lines represent the multipole decomposition confirming the statement that only multipoles with $m = 0, 4$ are involved by the symmetry properties. Numerical parameters: incident light wavelength $\lambda = 1550$ nm, refractive index at the fundamental frequency $n^{\omega} = 3.28$, at the 2ω $n^{\omega} = 3.56$

As a result, taking into account the lattice symmetry of GaAs crystal provided by $\chi^{(2)}_{\text{GaAs}}$ as well as the axial symmetry of the spherical particle, one can show that only $m = 0, \pm 4$ VSH are allowed in the second harmonic field produced from the right/ left circularly polarised incident light [46]. To confirm this statement, Fig. 4.2 shows the SHG efficiency (naturally defined as the fraction $\sigma_{\text{SHG}}/\sigma_{\text{geom}}$) depending on the particle radius normalized by the wavevector $k(\omega)$. The solid black line represents the total SHG efficiency, while dashed curves correspond to the multipole decomposition, where (m,n) notation was used on the right to address different multipoles that contribute to the total SHG efficiency.

Therefore, one can clearly see that the total efficiency is fully represented only via multipoles with $m = 0, 4$, therefore, indeed only these particular terms are allowed in the second harmonic scattered filed spectrum.

Going back to the expression for total torque presented in 4.27, we recall the fact that $m_i = 1$ for the polarization of the incident light we consider. Therefore, for VSH with $m = 0$, SH torque $T_z^{(2\omega)} = 0$, while $T_z^{(\omega)} > 0$, as a result, the corresponding term that goes to total torque is positive and provided only by the one that corresponds to the fundamental frequency ω. At the same time, for $m = 4$ harmonics, we have $2m_i - m = 2 - 4 = -2$, thus, $T_z^{(2\omega)} = -2 \cdot T_z^{(\omega)}$ and the contribution to total torque coming from this particular multipole is negative and equal to $-T_z^{(\omega)}$.

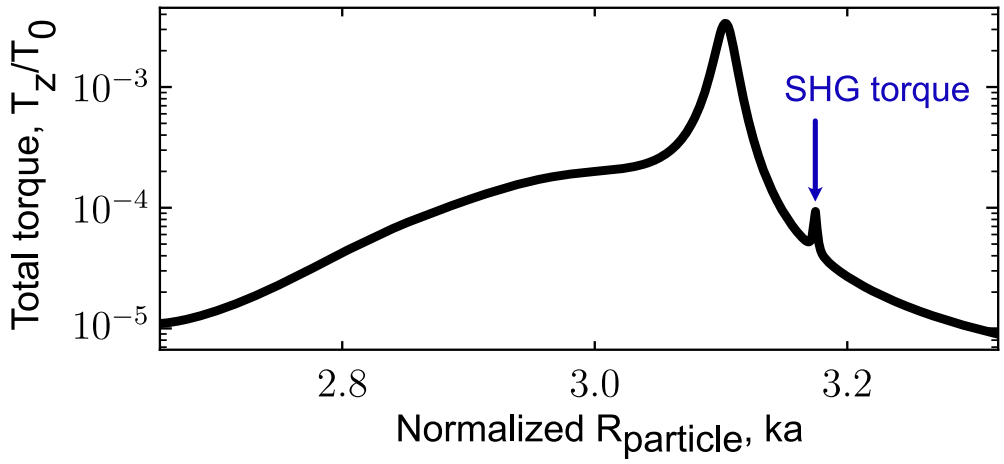

Figure 4.3 — Total optical torque acting on the spherical GaAs nanoparticle as a function of its radius. Due to the dominating contribution of $m = 0$ multipole modes, the total torque is fully positive

Finally, we compute the total torque acting on a resonant nanoparticle as a function of normalized particle radius shown in Fig. 4.3. Even though it was shown that for $m = 4$ multipoles the contribution to total torque is negative, total torque we obtain numerically is still fully positive. The reason for that is the dominating contribution to the SHG process coming from the harmonics with $m = 0$ (as illustrated in Fig. 4.2). At the same time, one can clearly see that the maximum values of the total torque correspond to the maximal values of the SH efficiency

as shown in Fig. 4.2, while the strongest contribution of the SH torque appears at $ka \approx 3.18$.

Overall, we indeed observe the emergence of non-linear optical torque acting on a Mie-resonant nanoparticle and induced by the second harmonic generation. However, even though the terms that correspond to SH torque are negative, total torque seems to be positive. At this point a natural question might appear, namely, whether it is possible to obtain negative total torque. The answer is yes [48], but goes beyond the scope of this work, however, we would like to highlight the general idea. First of all, it is quite intuitive that one needs to modify the SH scattered field such that the modes with $m = 4$ are sufficiently enhanced. To be more precise, changing the shape of the particle from spherical to cylindrical can lead to the emergence of quasi-bound states (qBIC) in the continuum, therefore, resulting in negative optical torque due to its dominating contribution in the scattered field spectrum. As was already mentioned, a more detailed analysis of this question is presented in [48].

CONCLUSION

To summarize, we demonstrated several optomechanical applications related to trapping and rotating properties of resonant Mie-nanoparticles. To be more precise, in the following work we:

1) Investigated the total force acting on a resonant nanoparticle trapped at the node of the standing wave electric field. We derived the analytical expression for total trap stiffness based on the multipole decomposition and identify the main multipole forces for stable trapping at low-intensity spot related to the particle's radius and the wavelength of the standing wave. It was shown that at the node of the electric field stable trapping is provided by magnetic multipole forces, while for trapping at the node of magnetic field one could expect electric multipoles to provide trapping in the same way.

2) Studied the formation of the bottle-beam trap and observed stable trapping at minimum intensity spot. Explicitly calculated axial and transverse forces allowed us to determine the relative particle's radius and beam wavelength such that stable trapping can be observed. The multipole decomposition approach showed that magnetic dipole, electric dipole and magnetic quadrupole forces stand for trapping at minimum intensity spot along z-direction, while the transverse trapping is achieved mainly by the electric and magnetic quadrupole forces.

3) Demonstrated the emergence of optical torque acting on a perfect spherical nanoparticle induced by the second harmonic generation. We explicitly derived the fundamental and the SH torque components that forms total torque. In addition, we presented a concrete example how the expression we derived can be implemented to calculate torque acting on a GaAs nanoparticle. The following results are included in arxiv publication [48] that was recently accepted in Physics Review Letters.

We believe that our findings open several prospective directions for studying optomechanical properties of resonant nanoparticles. Here we are

especially interested in the ones related to optical trapping, namely, regarding the optimization of system parameters for a real experiment. In other words, taking into account the natural constraints on incident beam power, desired trapping wavelength, refractive index of a particle as well as its common radius, the question on how to maximise stability of trapping, namely, to increase the value of total positive stiffness, still remains to be open and quite non-trivial. At the same time, since one of the main motivations to use bottle-beam traps is minimising the internal temperature of a trapped particle, its explicit calculation or, for instance, an estimation based on the black body radiation, could convince experimentalists to continue developing optical levitation techniques with resonant nanoparticles.

BIBLIOGRAPHY

1. Functional Meta-Optics and Nanophotonics Governed by Mie Resonances [Text] / S. Kruk, Y. Kivshar, [et al.] // ACS Photonics. — 2017. — Nov. — Vol. 4, no. 11. — P. 2638—2649.

2. Meta-Optics with Mie Resonances [Text] / Y. Kivshar, A. Miroshnichenko, [et al.] // Optics &. Photonics News, OPN. — 2017. — Jan. — Vol. 28, no. 1. — P. 24—31.

3. The Mie Theory [Text]. — Berlin, Germany : Springer, 2012. — URL: https://link.springer.com/book/10.1007/978-3-642-28738-1.

4. Levitated Optomechanics with Meta-Atoms [Text] / S. Lepeshov, N. Meyer, P. Maurer, [et al.] // arXiv. — 2022. — Nov. — eprint: 2211.08235.

5. Subwavelength dielectric resonators for nonlinear nanophotonics [Text] / K. Koshelev, S. Kruk, E. Melik-Gaykazyan, [et al.] // Science. — 2020. — Jan. — Vol. 367, no. 6475. — P. 288—292. — eprint: 31949078.

6. Nonlinear optics in all-dielectric nanoantennas and metasurfaces: a review [Text] / B. Sain, C. Meier, T. Zentgraf, [et al.] // Advanced Photonics, Vol. 1, Issue 2. Vol. 1. — SPIE, 04/2019. — P. 024002.

7. Acceleration and Trapping of Particles by Radiation Pressure [Text] / A. Ashkin [et al.] // Phys. Rev. Lett. — 1970. — Jan. — Vol. 24, no. 4. — P. 156—159.

8. Optical Levitation by Radiation Pressure [Text] / A. Ashkin, J. M. Dziedzic, [et al.] // Appl. Phys. Lett. — 1971. — Oct. — Vol. 19, no. 8. — P. 283—285.

9. Stability of optical levitation by radiation pressure [Text] / A. Ashkin, J. M. Dziedzic, [et al.] // Appl. Phys. Lett. — 1974. — June. — Vol. 24, no. 12. — P. 586—588.

10. Observation of a single-beam gradient force optical trap for dielectric particles [Text] / A. Ashkin, J. M. Dziedzic, J. E. Bjorkholm, [et al.] // Opt. Lett. — 1986. — May. — Vol. 11, no. 5. — P. 288—290.

11. 03/2023. — URL: https://www.nobelprize.org/uploads/2018/10/ashkin-lecture.pdf.

12. Optical tweezers in single-molecule experiments [Text] / A. Zaltron, M. Merano, G. Mistura, [et al.] // Eur. Phys. J. Plus. — 2020. — Nov. — Vol. 135, no. 11. — P. 1—33.

13. Optical tweezers in single-molecule biophysics [Text] / C. J. Bustamante, Y. R. Chemla, S. Liu, [et al.] // Nat. Rev. Methods Primers. — 2021. — Mar. — Vol. 1, no. 25. — P. 1—29.

14. Ten years of tension: single-molecule DNA mechanics [Text] / C. Bustamante, Z. Bryant, S. B. Smith, [et al.] // Nature. — 2003. — Jan. — Vol. 421. — P. 423—427.

15. Microfluidic Cell Sorting: A Review of the Advances in the Separation of Cells from Debulking to Rare Cell Isolation [Text] / I. V. C. Wyatt Shields, D. C. D. Reyes, P. G. P. Lpez, [et al.] // Lab Chip. — 2015. — Feb. — Vol. 15, no. 5. — P. 1230.

16. Versatile, facile and low-cost single-cell isolation, culture and sequencing by optical tweezer-assisted pool-screening [Text] / T. Xu, Y. Li, X. Han, [et al.] // Lab Chip. — 2022. — Dec. — Vol. 23, no. 1. — P. 125—135.

17. Preparation of hundreds of microscopic atomic ensembles in optical tweezer arrays [Text] / Y. Wang, S. Shevate, T. M. Wintermantel, [et al.] // npj Quantum Inf. — 2020. — June. — Vol. 6, no. 54. — P. 1—5.

18. Dynamic holographic optical tweezers [Text] / J. E. Curtis, B. A. Koss, D. G. Grier, [et al.] // Opt. Commun. — 2002. — June. — Vol. 207, no. 1. — P. 169—175.

19. Trapping Alkaline Earth Rydberg Atoms Optical Tweezer Arrays [Text] / J. T. Wilson, S. Saskin, Y. Meng, [et al.] // Phys. Rev. Lett. — 2022. — Jan. — Vol. 128, no. 3. — P. 033201.

20. Quantum Computing with Trapped Ions quantum computing [Text] / W. Lange [et al.] // Computational Complexity. — New York, NY, USA : Springer, New York, NY, 2012. — P. 2406—2436.

21. Demonstration of the trapped-ion quantum CCD computer architecture [Text] / J. M. Pino, J. M. Dreiling, C. Figgatt, [et al.] // Nature. — 2021. — Apr. — Vol. 592. — P. 209—213.

22. Optical levitation and feedback cooling of a nanoparticle at subwavelength distances from a membrane [Text] / R. Diehl, E. Hebestreit, R. Reimann, [et al.] // Phys. Rev. A. — 2018. — July. — Vol. 98, no. 1. — P. 013851.

23. Cooling of a levitated nanoparticle to the motional quantum ground state [Text] / U. Deli, M. Reisenbauer, K. Dare, [et al.] // Science. — 2020. — Feb. — Vol. 367, no. 6480. — P. 892—895.

24. Efficient generation of optical bottle beams [Text] / Y. Xiao, Z. Yu, R. A. Wambold, [et al.] // Nanophotonics. — 2021. — Sept. — Vol. 10, no. 11. — P. 2893—2901.

25. Polarization-induced torque in optical traps [Text] / S. H. Simpson, D. C. Benito, S. Hanna, [et al.] // Phys. Rev. A. — 2007. — Oct. — Vol. 76, no. 4. — P. 043408.

26. *Brasselet*, *E.* Optical angular manipulation of liquid crystal droplets in laser tweezers [Text] / E. Brasselet, S. Juodkazis // J. Nonlinear Opt. Phys. Mater. — 2009. — June. — Vol. 18, no. 02. — P. 167—194.

27. Radiation torque on a sphere caused by a circularly-polarized electromagnetic wave [Text] / P. L. Marston, J. H. Crichton, [et al.] // Phys. Rev. A. — 1984. — Nov. — Vol. 30, no. 5. — P. 2508—2516.

28. Force and torque on an electric dipole by spinning light fields [Text] / A. Canaguier-Durand, A. Cuche, C. Genet, [et al.] // Phys. Rev. A. — 2013. — Sept. — Vol. 88, no. 3. — P. 033831.

29. Linear momentum increase and negative optical forces at dielectric interface [Text] / V. Kajorndejnukul, W. Ding, S. Sukhov, [et al.] // Nat. Photonics. — 2013. — Oct. — Vol. 7. — P. 787—790.

30. How light absorption modifies the radiative force on a microparticle in optical tweezers [Text] / W. H. Campos, J. M. Fonseca, J. B. S. Mendes, [et al.] // Appl. Opt. — 2018. — Sept. — Vol. 57, no. 25. — P. 7216—7224.

31. Clustering of Janus particles in an optical potential driven by hydrodynamic fluxes [Text] / S. M. Mousavi, I. Kasianiuk, D. Kasyanyuk, [et al.] // Soft Matter. — 2019. — July. — Vol. 15, no. 28. — P. 5748—5759.

32. Generalized lorenz-mie theories [Text]. Vol. 31 / G. Gouesbet, G. Gréhan, [et al.]. — Springer, 2011.

33. Fifth-order corrected electromagnetic field components for a fundamental Gaussian beam [Text] / J. P. Barton, D. R. Alexander, [et al.] // J. Appl. Phys. — 1989. — Oct. — Vol. 66, no. 7. — P. 2800—2802.

34. Absorption and scattering of light by small particles [Text] / C. F. Bohren, D. R. Huffman, [et al.]. — John Wiley & Sons, 2008.

35. Chiral optical tweezers for optically active particles in the T-matrix formalism [Text] / F. Patti, R. Saija, P. Denti, [et al.] // Sci. Rep. — 2019. — Jan. — Vol. 9, no. 29. — P. 1—10.

36. Optical tweezers computational toolbox [Text] / T. A. Nieminen, V. L. Y. Loke, A. B. Stilgoe, [et al.] // J. Opt. A: Pure Appl. Opt. — 2007. — July. — Vol. 9, no. 8. — S196.

37. T-matrix approach to calculating circular polarization of aggregates made of optically active materials [Text] / D. Mackowski, L. Kolokolova, W. Sparks, [et al.] // J. Quant. Spectrosc. Radiat. Transfer. — 2011. — July. — Vol. 112, no. 11. — P. 1726—1732.

38. Multipole Theory In Electromagnetism: Classical [Text] / R. Raab, O. De Lange, [et al.] // Quantum, And Symmetry Aspects, With Applications (International Series of Monographs on Physics)(Oxford University Press, USA, 2005). — 2005.

39. Multipole Engineering of Attractive-Repulsive and Bending Optical Forces [Text] / D. A. Kislov, E. A. Gurvitz, V. Bobrovs, [et al.] // Adv. Photonics Res. — 2021. — Sept. — Vol. 2, no. 9. — P. 2100082.

40. Classical Electrodynamics [Text]. Vol. 1 / J. D. Jackson [et al.]. — 1998.

41. Principles of Nano-Optics [Text]. Vol. 1 / L. Novotny, B. Hetch, [et al.]. — 2010.

42. Theoretical determination of net radiation force and torque for a spherical particle illuminated by a focused laser beam [Text] / J. P. Barton, D. R. Alexander, S. A. Schaub, [et al.] // J. Appl. Phys. — 1989. — Nov. — Vol. 66, no. 10. — P. 4594—4602.

43. Radiation torque exerted on a uniaxial anisotropic sphere: Effects of various parameters [Text] / Z. Li, Z. Wu, T. Qu, [et al.] // Opt. Laser Technol. — 2014. — Dec. — Vol. 64. — P. 269—277.

44. Calculation of radiation force and torque exerted on a uniaxial anisotropic sphere by an incident Gaussian beam with arbitrary propagation and polarization directions [Text] / Z.-J. Li, Z.-S. Wu, Q.-C. Shang, [et al.] // Opt. Express. — 2012. — July. — Vol. 20, no. 15. — P. 16421—16435.

45. Radiation torque on nonspherical particles in the transition matrix formalism [Text] / F. Borghese, P. Denti, R. Saija, [et al.] // Opt. Express. — 2006. — Oct. — Vol. 14, no. 20. — P. 9508—9521.

46. Second-harmonic generation in Mie-resonant dielectric nanoparticles made of noncentrosymmetric materials [Text] / K. Frizyuk, I. Volkovskaya, D. Smirnova, [et al.] // Phys. Rev. B. — 2019. — Feb. — Vol. 99, no. 7. — P. 075425.

47. Tailoring Second-Harmonic Emission from (111)-GaAs Nanoantennas [Text] / J. Sautter, L. Xu, A. E. Miroshnichenko, [et al.] // Nano Lett. — 2019. — June. — Vol. 19, no. 6. — P. 3905—3911.

48. Nonlinearity-induced optical torque [Text] / I. Toftul, G. Fedorovich, D. Kislov, [et al.] // arXiv. — 2022. — Oct. — eprint: 2210.04021.